Author: Köhlinger, F.
Title: Weighing the dark : cosmological applications of gravitational lensing
Issue Date: 2016-09-28

5

KiDS-450: The tomographic weak lensing power spectrum and constraints on neutrinos and cosmological parameters

We present measurements of the weak gravitational lensing shear power spectrum based on $\approx$450 deg^2 of imaging data from the Kilo-Degree Survey (KiDS). We employ a direct quadratic estimator in two redshift bins and extract band powers of the redshift auto-correlation spectra and cross-correlation spectrum in the multipole range $76 \leq \ell \leq 1310$. The cosmological interpretation of the measured shear power spectra is performed in a Bayesian framework assuming a flat Λ cold dark matter model, while accounting for small residual uncertainties in the shear calibration, intrinsic alignments, and baryon feedback. This yields the constraint on the parameter combination $S_8 \equiv \sigma_8 \sqrt{\Omega_\mathrm{m}/0.3} = 0.742 \pm 0.057$. This result is in tension at 1.8σ with the constraint from *Planck* based on measurements of the cosmic microwave background radiation. For the extension of the fiducial model with a free total mass of three degenerate massive neutrinos we derive the upper limit $\Sigma m_\nu < 3.46$ eV at 95 per cent credibility from the lensing data only. However, a Bayesian model comparison does not yield any evidence for extending the baseline model with a free total neutrino mass.

F. Köhlinger and the KiDS Collaboration

5.1 Introduction

The current cosmological concordance model successfully describes observations spanning a wide range in cosmic volume from the cosmic microwave background (CMB) power spectrum (e.g. Planck Collaboration XIII 2015a), the Hubble diagram based on supernovae of type IA (SNIa; e.g. Riess et al. 2016), big bang nucleosynthesis (BBN; e.g. Fields & Olive 2006), to the distance scales inferred from baryon acoustic oscillations imprinted in the large-scale clustering of galaxies (BAO; e.g. BOSS Collaboration 2015). Based on Einstein's theory of general relativity and the application of the Copernican principle to the whole Universe, the Λ-dominated cold dark matter (ΛCDM) model requires in its simplest form only a handful of parameters to fit all current observational data. However, the physical nature of two of these parameters, dark matter and dark energy, is still unknown, although their energy densities at present are very well constrained by observations. Within current limits dark energy can sill be interpreted in terms of the cosmological constant Λ, but any observed deviation from a constant value will have profound consequences that might eventually even lead to a revision of our theory of gravity. The cosmological concordance model is also naturally linked to the standard model of particle physics and the discovery of the constituents of dark matter will make its revision inevitable. However, experiments have already shown another shortcoming of the standard model: the experimental discovery of neutrino oscillations (Super-Kamiokande Collaboration 1998; SNO Collaboration 2001, 2002) indicates that neutrinos possess mass, which is in direct contradiction to its fiducial predictions.

Massive neutrinos affect the growth of cosmological large-scale structure (e.g. Lesgourgues & Pastor 2006 and references therein for a review) and hence a measurement of the growth of large-scale structure yields a constraint on the total mass over all neutrino species (e.g. Palanque-Delabrouille et al. 2015) which is an important complementary constraint to particle physics experiments.

Cosmic shear, i.e. the weak gravitational lensing due to all intervening cosmic large-scale structure between an observer and all sources along the line-of-sight, presents a viable tool to study the evolution of the dark species. However, the tiny coherent image distortions, the shear, of background sources caused by the bending of their emitted light perpendicular to the line-of-sight of a foreground mass need to be studied in statistically large samples. Hence, wide-field surveys covering increasingly more volume in the sky are the current and future strategy for improving the precision of the measurements. Data from large weak-lensing surveys such as the Kilo-Degree Survey (KiDS;[1] de Jong et al. 2013, 2015; Kuijken et al. 2015), the Subaru Hyper SuprimeCam lensing survey[2], and the Dark Energy Survey (DES;[3] Jarvis et al. 2015) are currently building up. These surveys are expected to reach coverage on the order of (several) 1000 deg^2 within the next few years, which presents an order of magnitude increase compared to currently available survey data (Erben et al. 2013; Kuijken et al. 2015; Jarvis et al. 2015). Eventually, close to all-sky surveys will be carried out over the next decade by the ground based Large Synoptic Survey Telescope[4] (Ivezic et al. 2008)) and the spaceborne *Euclid*[5] satellite (Laureijs et al. 2011) and the *Wide Field Infrared Survey Telescope*.[6]

The cosmic shear signal as a function of redshift is sensitive to the growth of structure and the geometry of the Universe and studying its redshift dependence allows us to infer the

---

[1] `kids.strw.leidenuniv.nl`

[2] `www.naoj.org/Projects/HSC/`

[3] `www.darkenergysurvey.org`

[4] `www.lsst.org`

[5] `www.euclid-ec.org`

[6] `wfirst.gsfc.nasa.gov`

expansion rate as well as the clustering behaviour of cosmic species such as cold dark matter, massive neutrinos, and dark energy.

There are several approaches to measure cosmic shear; the most common one to date is based on the two-point statistics of real-space correlation functions (e.g. Kilbinger 2015 for a recent review). The redshift dependence is either considered by performing the cosmic shear measurement in tomographic redshift slices (e.g. Benjamin et al. 2013, Heymans et al. 2013, Becker et al. 2015) or by employing redshift-dependent spherical Bessel functions (Kitching et al. 2014). An alternative and mathematically equivalent approach is to switch to Fourier space and measure the power spectrum of cosmic shear instead. One particular advantage of direct shear power spectrum estimators over correlation-function measurements is that the power spectrum measurements are significantly less correlated on all scales. This is very important for the clean study of scale-dependent signatures such as, for example, those caused by massive neutrinos. In addition, proper modelling is needed on non-linear scales in order to avoid any bias in the cosmological parameters. This, however, is complicated because of the feedback effects of baryon physics on the matter power spectrum of which we still have an insufficient understanding (Semboloni et al. 2011, 2013). Direct power spectrum estimators have already been applied to data, the quadratic estimator for example to the COMBO-17 dataset (Brown et al. 2003) and the GEMS dataset (Heymans et al. 2005). In a more recent study Lin et al. (2012) applied a quadratic estimator and a direct pseudo-$C(\ell)$ estimator based on Hikage et al. (2011) to data from the SDSS Stripe 82. However, the direct power spectrum estimators in these studies did not employ a tomographic approach. This was done for the first time in **Chapter 4**, where we extended the quadratic estimator formalism to include redshift bins and applied it to shear catalogues from the lensing analysis of the Canada–France–Hawaii Telescope Legacy Survey (CFHTLenS; Erben et al. 2013, Heymans et al. 2012, Hildebrandt et al. 2012).

Previous results from a six bin tomographic correlation-function analysis of CFHTLenS (Heymans et al. 2013) and a re-analysis by Joudaki et al. (2016) incorporating new knowledge regarding systematic errors in the photometric redshift distributions (Choi et al. 2015) found cosmological parameter constraints to be in tension with CMB based results from Planck Collaboration XIII (2015a). However, our quadratic estimator re-analysis of CFHTLenS from **Chapter 4** using only two tomographic bins at higher redshifts and incorporating larger angular scales, did not reveal any tension with results from *Planck*, which can be attributed though to increased errorbars due to the more conservative analysis. Similarly, results from a correlation-function analysis from DES (DES Collaboration 2015) are not in tension with *Planck* either. However, due to the small area coverage of the science verification data their errorbars are significantly larger compared to results from CFHTLenS.

Results from other low-redshift probes measuring the growth rate such as galaxy cluster counts (e.g. Planck Collaboration XXIV 2015b, de Haan et al. 2016) or redshift space distortions (e.g. Beutler et al. 2014, Samushia et al. 2014, Gil-Marín et al. 2016) consistently find a lower amplitude of fluctuations (parametrized as σ_8, the root-mean-square variance in spheres of $8\,h^{-1}$Mpc) at a given matter density ($\Omega_{\rm m}$) with respect to results from *Planck*. Hence, there are also claims in the literature (e.g. Spergel et al. 2015, Addison et al. 2016, Riess et al. 2016) that systematic errors that are yet unaccounted for in the *Planck* analysis might be the reason for the observed tension.

An intermediate data release from the ongoing KiDS covering an area of about $450\,\mathrm{deg}^2$ presents an independent dataset to re-evaluate whether or not cosmic shear results are in tension with *Planck*. The imaging data are taken with a combination of camera and telescope designed to yield among the best shear data quality attainable from the ground and the setup is different from the one employed for CFHTLenS. Latest results from a 4-bin tomographic correlation-function analysis employing these data (Hildebrandt et al. 2016) are in tension with results from *Planck*, but agree well with results from other low-redshift probes. At the moment it is yet too premature to decide whether the tension between *Planck* and low-redshift probes is due to internal systematics that are yet unaccounted for in each probe (e.g. for low-redshift probes the proper modelling of the matter power spectrum at very non-linear scales is a concern) or if the tension is due to new physics implying that the current cosmological concordance model is incomplete and requires physical parameter extensions (e.g. Di Valentino et al. 2015).

In this paper we follow the fiducial analysis by Hildebrandt et al. (2016) closely but use the tomographic quadratic estimator instead to measure the cosmic shear power spectrum directly from the data over the same redshift range, using two tomographic bins. This presents an important cross-check of the robustness of the results derived with two independent data analysis pipelines and estimators employing the same shear catalogues. Moreover, we explore model extensions beyond ΛCDM which might alleviate or even strengthen the tension assuming that all systematic errors are properly accounted for.

The paper is organized as follows: in Section 5.2 we summarize the theory for cosmic shear power spectra and in Section 5.3 we present the quadratic estimator algorithm. Section 5.4 introduces the KiDS-450 dataset and the most important properties of the lensing source sample. In Section 5.5 we describe the calibrations applied to the measured shear signal. Section 5.6 summarizes the details of the employed covariance matrix of the data. In Section 5.7 we present the measured cosmic shear power spectra and show a qualitative comparison to correlation-function measurements. The cosmological interpretation of the cosmic shear power spectra is discussed in Section 5.8 before we summarize all results and conclude in Section 5.9.

5.2 Theory

A consequence of Einstein's principle of equivalence is the deflection of light due to mass. We call this gravitational lensing and in this paper we will specifically work in the framework of weak gravitational lensing. It is called weak because the gradient of the gravitational potential of a deflecting foreground mass only induces very weak but coherent distortions of background sources. The measurement of the image distortions is only possible in a statistical sense and requires to average over large samples of background galaxies due to the broad distribution of intrinsic ellipticities of galaxies. The very weak-lensing effect of all intervening mass between an observer and all sources along the line-of-sight is called cosmic shear. The resulting correlations of galaxy shapes can be used to study the evolution of the large-scale structure and therefore cosmic shear becomes an increasingly valuable tool for cosmology especially in the current era of large surveys (cf. Kilbinger 2015 for a recent review). For details on the theoretical foundations of (weak) gravitational lensing we refer the reader to the standard literature (e.g. Bartelmann & Schneider 2001).

The main observables in a weak-lensing survey are the shapes and (photometric) redshifts of galaxies. The measured galaxy shapes in terms of ellipticity components e_1, e_2 at angular positions $\boldsymbol{n}_i$ are binned into pixels $i = 1, ..., N_{\rm pix}$ and (photometric) redshift bins z_μ. Averaging then the ellipticities in each pixel yields estimates of the components of the spin-2 shear field, $\gamma_1(\boldsymbol{n}, z_\mu)$ and $\gamma_2(\boldsymbol{n}, z_\mu)$. Its Fourier decomposition can be written in the flat-sky limit as

$$\gamma_1(\boldsymbol{n}, z_\mu) \pm {\rm i}\gamma_2(\boldsymbol{n}, {\rm z}_\mu) = \int \frac{{\rm d}^2\ell}{(2\pi)^2} \left[\kappa(\boldsymbol{\ell}, {\rm z}_\mu) \pm {\rm i}\beta(\boldsymbol{\ell}, {\rm z}_\mu)\right] {\rm W}(\boldsymbol{\ell}) {\rm e}^{\pm 2{\rm i}\varphi_\ell} {\rm e}^{{\rm i}\boldsymbol{\ell}\cdot\boldsymbol{n}} , \qquad (5.1)$$

with φ_ℓ denoting the angle between the two-dimensional vector $\boldsymbol{\ell}$ and the x-axis. For the lensing by density perturbations the convergence field κ contains all the cosmological information and the field β usually vanishes in the absence of systematics. In the subsequent analysis we will still extract it and treat it as a check for residual systematics in the data.

The Fourier transform of the pixel window function, $W(\boldsymbol{\ell})$, can be written out as

$$W(\boldsymbol{\ell}) = j_0\left(\frac{\ell_x \sigma_{\mathrm{pix}}}{2} \cos\varphi_\ell\right) j_0\left(\frac{\ell_y \sigma_{\mathrm{pix}}}{2} \sin\varphi_\ell\right), \tag{5.2}$$

where $j_0(x) = \sin(x)/x$ is the zeroth-order spherical Bessel function and σ_{pix} is the side length of a square pixel in radians.

The shear correlations between pixels $\boldsymbol{n}_i$ and $\boldsymbol{n}_j$ and tomographic bins μ and ν can be expressed in terms of their power spectra and they define the shear-signal correlation matrix (Hu & White 2001):

$$\mathbf{C}^{\mathrm{sig}} = \langle \gamma_a(\boldsymbol{n}_i, z_\mu)\gamma_b(\boldsymbol{n}_j, z_\nu)\rangle, \tag{5.3}$$

with components

$$\begin{aligned}
\langle\gamma_{1i\mu}\gamma_{1j\nu}\rangle &= \int \frac{\mathrm{d}^2\ell}{(2\pi)^2}\left[C^{\mathrm{EE}}_{\mu\nu}(\ell)\cos^2 2\varphi_\ell + C^{\mathrm{BB}}_{\mu\nu}(\ell)\sin^2 2\varphi_\ell - C^{\mathrm{EB}}_{\mu\nu}(\ell)\sin 4\varphi_\ell\right] W^2(\boldsymbol{\ell})\mathrm{e}^{\mathrm{i}\boldsymbol{\ell}\cdot(\boldsymbol{n}_\mathrm{i}-\boldsymbol{n}_\mathrm{j})}, \\
\langle\gamma_{2i\mu}\gamma_{2j\nu}\rangle &= \int \frac{\mathrm{d}^2\ell}{(2\pi)^2}\left[C^{\mathrm{EE}}_{\mu\nu}(\ell)\sin^2 2\varphi_\ell + C^{\mathrm{BB}}_{\mu\nu}(\ell)\cos^2 2\varphi_\ell + C^{\mathrm{EB}}_{\mu\nu}(\ell)\sin 4\varphi_\ell\right] W^2(\boldsymbol{\ell})\mathrm{e}^{\mathrm{i}\boldsymbol{\ell}\cdot(\boldsymbol{n}_\mathrm{i}-\boldsymbol{n}_\mathrm{j})}, \\
\langle\gamma_{1i\mu}\gamma_{2j\nu}\rangle &= \int \frac{\mathrm{d}^2\ell}{(2\pi)^2}\left[\tfrac{1}{2}\left(C^{\mathrm{EE}}_{\mu\nu}(\ell) - C^{\mathrm{BB}}_{\mu\nu}(\ell)\right)\sin 4\varphi_\ell + C^{\mathrm{EB}}_{\mu\nu}(\ell)\cos 4\varphi_\ell\right] W^2(\boldsymbol{\ell})\mathrm{e}^{\mathrm{i}\boldsymbol{\ell}\cdot(\boldsymbol{n}_\mathrm{i}-\boldsymbol{n}_\mathrm{j})}.
\end{aligned} \tag{5.4}$$

In the equations above we introduced the decomposition of the shear field into curl-free and curl components, i.e. E- and B-modes, respectively. In the absence of systematic errors and shape noise, the cosmological signal is contained in the E-modes and their power spectrum is equivalent to the convergence power spectrum, i.e. $C^{\mathrm{EE}}(\ell) = C^{\kappa\kappa}(\ell)$ and $C^{\mathrm{BB}}(\ell) = 0$. Shot noise will generate equal power in E- and B-modes. The cross-power between E- and B-modes, $C^{\mathrm{EB}}(\ell)$, is expected to be zero because of the parity invariance of the shear field.

The theoretical prediction for the convergence power spectrum per redshift-bin correlation μ, ν can be calculated in the Limber approximation (Limber 1954) as

$$C^{\mathrm{EE}}_{\mu\nu}(\ell) = \int_0^{\chi_\mathrm{H}} \mathrm{d}\chi\, \frac{q_\mu(\chi) q_\nu(\chi)}{f^2_\mathrm{K}(\chi)} P_\delta\left(k = \frac{\ell}{f_\mathrm{K}(\chi)}; \chi\right), \tag{5.5}$$

which depends on the radial comoving distance χ, the distance to the horizon χ_H, the angular diameter distance $f_\mathrm{K}(\chi)$, and the three-dimensional matter power spectrum $P_\delta(k;\chi)$.

The weight functions $q_\mu(\chi)$ depend on the lensing kernels and hence they are a measure for the lensing efficiency in each tomographic bin μ:

$$q_\mu(\chi) = \frac{3\Omega_\mathrm{m} H_0^2}{2c^2}\frac{f_\mathrm{K}(\chi)}{a(\chi)}\int_\chi^{\chi_\mathrm{H}} \mathrm{d}\chi'\, n_\mu(\chi')\frac{f_\mathrm{K}(\chi'-\chi)}{f_\mathrm{K}(\chi')}, \tag{5.6}$$

where $a(\chi)$ is the scale factor and the source redshift distribution is denoted as $n_\mu(\chi)\,\mathrm{d}\chi = n_\mu(z)\,\mathrm{d}z$. It is normalized such that $\int \mathrm{d}\chi\, n_\mu(\chi) = 1$.

5.3 Quadratic estimator

There are two main techniques to extract the shear power spectrum directly from the data: one is based on a maximum-likelihood technique and employs a quadratic estimator (Bond et al.

1998; Seljak 1998; Hu & White 2001), whereas the other approach uses a pseudo spectrum (also pseudo-$C(\ell)$; Hikage et al. 2011). Moreover, there are pseudo-$C(\ell)$ methods that are based on correlation-function measurements (e.g. Becker et al. 2015). These present a hybrid approach and do not directly estimate the power spectrum from the shear data.

Here we summarize the quadratic estimator algorithm applied to cosmic shear including its extension to tomographic bins. For that we follow the original literature (Hu & White 2001; Lin et al. 2012) and the description in **Chapter 4**.

The likelihood of the measured shear field in terms of band powers $\mathcal{B}$ is assumed to be Gaussian over most scales of interest for our analysis, i.e.

$$\mathcal{L} = \frac{1}{(2\pi)^N |\mathbf{C}(\mathcal{B})|^{1/2}} \exp\left[-\tfrac{1}{2}\, \boldsymbol{d}^{\mathrm{T}} [\mathbf{C}(\mathcal{B})]^{-1} \boldsymbol{d}\right]. \tag{5.7}$$

The data vector $\boldsymbol{d}$ with components

$$d_{\mu a i} = \gamma_a(\boldsymbol{n}_i,\ z_\mu) \tag{5.8}$$

contains both components of the measured shear γ_a per pixel $\boldsymbol{n}_i$ for each redshift bin z_μ. The covariance matrix $\mathbf{C}$ is written as the sum of the cosmological signal $\mathbf{C}^{\mathrm{sig}}$ (cf. equation 5.3 and the noise $\mathbf{C}^{\mathrm{noise}}$.

As long as the pixel noise of the detector is uncorrelated, the noise matrix can be assumed to be diagonal, i.e. shape noise is neither correlated between different pixels $\boldsymbol{n}_i$, $\boldsymbol{n}_j$ and shear components γ_a, γ_b, nor between different redshift bins z_μ, z_ν:

$$\mathbf{C}^{\mathrm{noise}} = \frac{\sigma_e^2}{N_{i\mu}} \delta_{ij}\delta_{ab}\delta_{\mu\nu}\,, \tag{5.9}$$

where σ_e denotes the root-mean-square intrinsic ellipticity per ellipticity component for all the galaxies and $N_{i\mu}$ is the effective number of galaxies per pixel i in redshift bin z_μ.[7]

As noted above we approximate the angular power spectra $C^{\vartheta}_{\mu\nu}(\ell)$ with piecewise constant band powers $\mathcal{B}_{\zeta\vartheta\beta}(\ell)$ of type $\vartheta \in (\mathrm{EE}, \mathrm{BB}, \mathrm{EB})$ that span a range of multipoles ℓ within the band β. Note that the index ζ runs only over *unique* redshift bin correlations: for n_z redshift bins there are only $n_z(n_z+1)/2$ unique correlations because $z_\mu \times z_\nu = z_\nu \times z_\mu$. Hence, the components of the cosmic signal covariance matrix can be decomposed into a linear combination of these band powers:

$$C^{\mathrm{sig}}_{(\mu\nu)(ab)(ij)} = \sum_{\zeta,\vartheta,\beta} \mathcal{B}_{\zeta\vartheta\beta} M_{\zeta(\mu\nu)} \int_{\ell\in\beta} \frac{\mathrm{d}\ell}{2(\ell+1)} \left[w_0(\ell) I^{\vartheta}_{(ab)(ij)} + \tfrac{1}{2}\, w_4(\ell) Q^{\vartheta}_{(ab)(ij)}\right]. \tag{5.10}$$

The geometry of the shear field, including its Fourier-space decomposition and masks, is encoded in the above expression written in square brackets. The matrices $\mathbf{M}_\zeta$ are required for mapping the redshift-bin indices μ, ν to the unique correlations ζ possible between those. Explicit expressions for these matrices and the matrices $\mathbf{I}^{\vartheta}$ and $\mathbf{Q}^{\vartheta}$ can be found in Appendix 4.A.

In order to find the best-fitting band powers $\mathcal{B}_{\zeta\vartheta\beta}$ and the cosmic signal $\mathbf{C}^{\mathrm{sig}}$ that describes the measured shear data the best, we employ a Newton–Raphson optimization. The algorithm finds the root of $\mathrm{d}\mathcal{L}/\mathrm{d}\mathcal{B}_A = 0$ (Bond et al. 1998; Seljak 1998), i.e. its maximum-likelihood solution, by iteratively stepping through the expression $\mathcal{B}_{\mathrm{i}+1} = \mathcal{B}_{\mathrm{i}} + \delta\mathcal{B}$ in which $\delta\mathcal{B}$ is calculated in each step as

$$\delta\mathcal{B}_A \propto \sum_B \tfrac{1}{2} (\mathbf{F}^{-1})_{AB}\, \mathrm{Tr}[(\boldsymbol{d}\boldsymbol{d}^{\mathrm{T}} - \mathbf{C})(\mathbf{C}^{-1}\mathbf{D}_A\mathbf{C}^{-1})]\,. \tag{5.11}$$

---

[7] The effective number of galaxies per pixel can be calculated using equation (5.17) multiplied by the area of the pixel Ω.

In the following we simplify our notation by introducing the superindex A for a particular combination of indices $(\zeta\vartheta\beta)$. The matrices $\mathbf{D}_A$ are derivatives of the full covariance matrix with respect to any band-power combination. A rigorous definition of $\mathbf{D}_A$ can again be found in Appendix 4.A. The elements of the Fisher matrix $\mathbf{F}$ can be calculated as

$$F_{AB} = \frac{1}{2}\,\mathrm{Tr}(\mathbf{C}^{-1}\mathbf{D}_A\mathbf{C}^{-1}\mathbf{D}_B)\,. \tag{5.12}$$

An important point for the subsequent cosmological analysis is the estimation of the band-power covariance. The inverse of the Fisher matrix was used in previous work (cf. Hu & White 2001; Lin et al. 2012) as an approximation of the true covariance. This, however, holds only in the Gaussian limit. In this analysis we use a covariance matrix based on an analytical calculation, which is discussed in more detail in Section 5.6.

For that calculation, but also for a proper comparison of theory to data in the subsequent cosmological analysis, we also have to take into account that each measured band power $\mathcal{B}_A = \mathcal{B}_{\zeta\vartheta\beta}$ samples the corresponding power spectrum with its own window function. For a general estimator we can relate the expectation value of the measured band power, $\langle\mathcal{B}_{\zeta\vartheta\beta}\rangle$, to the power spectrum at integer multipole through the band-power window function $W_{A(\zeta\vartheta)}(\ell)$ (cf. Knox 1999; Lin et al. 2012), i.e.

$$\langle\mathcal{B}_{\zeta\vartheta\beta}\rangle = \sum_{\ell} W_{(\zeta\vartheta\beta)(\zeta\vartheta)}(\ell)\mathcal{B}_{\zeta\vartheta}(\ell)\,, \tag{5.13}$$

where $W_{(\zeta\vartheta\beta)(\zeta\vartheta)}(\ell)$ denotes the elements of the block diagonal of $W_{A(\zeta\vartheta)}(\ell)$ (A is again a superindex for single indices over the band types, unique redshift correlations and bands). The sum is calculated for integer multipoles ℓ in the range $10 \leq \ell \leq 3000$ since the cosmological analysis is intended to use multipoles in the range $76 \leq \ell \leq 2300$ (cf. Section 5.4). Therefore, the lowest multipole for the summation should extend slightly below $\ell_{\mathrm{field}} = 76$ and the highest multipole should include multipoles beyond $\ell = 2300$ in order to capture the full behaviour of the band window function below and above the lowest and highest bands, respectively.

The elements of the window function matrix can be derived as (cf. Lin et al. 2012)

$$W_{A(\zeta\vartheta)}(\ell) = \sum_{B} \frac{1}{2}(\mathbf{F}^{-1})_{AB}T_{B(\zeta\vartheta)}(\ell)\,, \tag{5.14}$$

where $\mathbf{F}^{-1}$ denotes the inverse of the Fisher matrix (cf. equation 5.12). The trace matrix $\mathbf{T}$ is defined as

$$T_{A(\zeta\vartheta)}(\ell) = \mathrm{Tr}[\mathbf{C}^{-1}\mathbf{D}_A\mathbf{C}^{-1}\mathbf{D}_{\zeta\vartheta}(\ell)]\,. \tag{5.15}$$

The derivative $\mathbf{D}_{\zeta\vartheta}(\ell)$ denotes the derivative of the full covariance $\mathbf{C}$ with respect to the power at a single multipole ℓ (per band type ϑ and unique redshift correlation ζ). We write it out explicitly in Appendix 5.A (cf. equation 5.32).[8]

5.4 KiDS-450 measurements

In the following analysis we use the KiDS-450 dataset and only provide a concise summary of it here. For full details we refer the reader to Hildebrandt et al. (2016) and references therein.

---

[8] Note that the definition of $\mathbf{D}_{\zeta\vartheta}(\ell)$ has changed with respect to the one presented in **Chapter 4**. This is due to the fact that in the previous analysis we only needed the EE to EE part of the band window matrix for convolving the cosmological signal prediction with it. The approach of an analytical covariance, however, requires us to calculate the full band window matrix with all possible cross-terms, which is now fully accounted for by the new notation presented here in this paper.

KiDS is an ongoing ESO optical survey which will eventually cover 1500 deg^2 in four bands (u, g, r, and i). It is carried out using the OmegaCAM CCD mosaic camera mounted at the Cassegrain focus of the VLT Survey Telescope (VST). The combination of camera and telescope was specifically designed for weak-lensing studies and hence results in small camera shear and an almost round and well-behaved point spread function (PSF). The data processing pipeline from individual exposures in multiple colours to photometric redshift estimates employs the ASTRO-WISE system (Valentijn et al. 2007; Begeman et al. 2013). For the lensing-specific data reduction of the r-band images THELI (Erben et al. 2005, 2009, 2013; Schirmer 2013) is used. Finally, the galaxy shapes are measured from the THELI-processed data with a new version of *lens*fit described in Fenech Conti et al. (2016). The full description of the pipeline for previous data releases of KiDS (DR1/2) is documented in de Jong et al. (2015) and Kuijken et al. (2015). All subsequent improvements applied to the data processing for KiDS-450 are summarized in Hildebrandt et al. (2016). The *lens*fit-specific updates including a description of the extensive image simulations for shear calibrations at the sub-percent level are documented in Fenech Conti et al. (2016).

The interpretation of the cosmic shear signal also requires accurate and precise redshift distributions, $n(z)$ (cf. equation 5.6). For the estimation of photometric redshifts the code BPZ (Benítez 2000) is used following the description in Hildebrandt et al. (2012). In previous KiDS and CFHTLenS analyses the stacked $n(z)$ based on the redshift probability distributions of individual galaxies, $P(z)$, as estimated by BPZ was used for that purpose. However, the output of photometric redshift estimation codes such as BPZ is biased at a level that is intolerable for current and especially future cosmic shear studies (cf. Newman et al. 2015; Choi et al. 2015 for a discussion).

Therefore, Hildebrandt et al. (2016) employ a weighted direct calibration (‘DIR’) of photometric redshifts with spectroscopic redshifts. This calibration method employs several spectroscopic redshift catalogues from surveys overlapping with KiDS, which are described in detail in Hildebrandt et al. (2016). In practice, spectroscopic redshift catalogues are neither complete nor a representative sub-sample of the photometric redshift catalogues currently used in cosmic shear studies. In order to alleviate these practical shortcomings the photometric redshift distributions and the spectroscopic redshift distributions are re-weighted in a multi-dimensional magnitude space, so that the volume density of objects in this magnitude space matches between photometric and spectroscopic catalogues (Lima et al. 2008). The direct calibration is further cross-checked with two additional methods and found to yield robust and precise estimates of the photometric redshift distribution of the galaxy source sample (cf. Hildebrandt et al. 2016 for details).

The fiducial KiDS-450 dataset consists of 454 individual ≈1 deg^2 tiles (cf. fig. 1 from Hildebrandt et al. 2016). The median seeing is 0.66 arcsec and no r-band image has a seeing larger than 0.96 arcsec. Since the observations prioritized increasing the overlap with the spectroscopic GAMA survey (Driver et al. 2011) the tiles are grouped into five patches (and corresponding catalogues) covering an area of ≈450 deg^2 in total. Due to stellar haloes or artefacts in the images the total area of KiDS-450 is reduced to an effective area usable for lensing of about 360 deg^2. Since the catalogue for an individual KiDS patch does not only consist of one contiguous (GAMA) field but also contains long stripes (e.g. 1 deg by several degrees) or individual tiles due to the pointing strategy, we exclude these disconnected tiles from our analysis, which amounts to a reduction in effective area by ≈36 deg^2 compared to Hildebrandt et al. (2016). Moreover, the individual patches are quite large resulting in long run-times for the signal extraction. Therefore, we split each individual KiDS patch further into two or three subpatches yielding 13 subpatches in total with an effective area of 323.9 deg^2. Each subpatch contains a comparable number of individual tiles and the splitting into subpatches was performed along borders that do not split individual tiles, because a single tile represents the smallest data unit for systematic checks and further quality control tests.

The coordinates in the catalogues are given in a spherical coordinate system measured in right ascension α and declination δ. Before we pixelize each subpatch into shear pixels, we first deproject the spherical coordinates into flat coordinates using a tangential plane projection (also known as gnomonic projection). The central point for the projection of each subpatch, i.e. its tangent point, is calculated as the intersection point of the two great circles spanned by the coordinates of the edges of the subpatch.

The shear components g_a per pixel at position $\boldsymbol{n} = (x_c, y_c)$ are estimated from the ellipticity components e_a inside that pixel:

$$g_a(x_\mathrm{c}, y_\mathrm{c}) = \frac{\sum_i w_i e_{a,i}}{\sum_i w_i} , \tag{5.16}$$

where the index a labels the two shear and ellipticity components, respectively, and the index i runs over all objects inside the pixel. The ellipticity components e_a and the corresponding weights w are computed during the shape measurement with *lens*fit and they account both for the intrinsic shape noise and measurement errors.

For the position of the average shear we take the centre of the pixel (hence the subscript ‘c’ in the coordinates). Considering the general width of our multipole band powers it is justified to assume that the galaxies are uniformly distributed in each shear pixel. Finally, we define distances $r_{ij} = |\boldsymbol{n}_i - \boldsymbol{n}_j|$ and angles $\varphi = \arctan(\Delta y/\Delta x)$ between shear pixels i, j which enter in the quadratic estimator algorithm (cf. Section 5.3).

The lowest scale of the multipole band powers that we extract is in general set by the largest separation θ_max possible between two shear pixels in each subpatch. In a square-field that would correspond to the diagonal separation of the pixels in the corners of the patch. However, this would yield only two independent realizations of the corresponding multipole ℓ_min. Hence, defining the lowest physical multipole ℓ_field as corresponding to the distance between two pixels on opposite sides of the patch ensures that there exist many independent realizations of that multipole so that a measurement thereof is statistically meaningful. In general, the subpatches used in this analysis are not square but rectangular and hence we follow the conservative approach of defining ℓ_field corresponding to the shorter side length of the rectangle. Choosing then the shortest side length among all 13 subpatches yields $\ell_\mathrm{field} = 76$ corresponding to a distance $\theta \approx 4\overset{\circ}{.}74$. The lowest multipole over all subpatches is $\ell_\mathrm{min} = 34$ corresponding to a distance $\theta \approx 10\overset{\circ}{.}5$ but we set the lower border of the first band power even lower to $\ell = 10$. That is because the quadratic estimator approach allows us to account for any leftover DC offset, i.e. a non-zero mean amplitude, in the signal by including even lower multipoles than ℓ_min in the first band power (cf. Section 5.5). The highest multipole ℓ_max available for the data analysis is set by the side length of the shear pixels. The total number of shear pixels in the analysis is also a critical parameter for the run-time of the algorithm because it sets together with the number of unique redshift correlations and the duality of the shear components the dimensionality of the fundamental covariance matrix (cf. equation 5.3). Moreover, Gaussianity is one of the assumptions behind the quadratic estimator which naturally limits the highest multipole to the mildly non-linear regime (cf. Hu & White 2001). Hence, we set $\sigma_\mathrm{pix} = 0\overset{\circ}{.}14$ corresponding to a maximum multipole $\ell_\mathrm{pix} = 2571$. However, the borders of the last band should extend to at least $2\ell_\mathrm{pix} \approx 5150$ due to the increasingly oscillatory behaviour of the pixel window function (cf. equation 5.2) close to and beyond ℓ_pix. The width of all intermediate bands should be at least $2\ell_\mathrm{field}$ in order to minimize the correlations between them (cf. Hu & White 2001). Given all these constraints we extract in total seven E-mode band powers over the range $10 \leq \ell \leq 5150$. However, for the

Table 5.1: Band-power intervals.

Band No.	ℓ-range	θ-range	Comments
1	10–75	2160.0–288.0 arcmin	(a), (b)
2	76–220	284.2–98.2 arcmin	–
3	221–420	98.0–51.4 arcmin	–
4	421–670	51.3–32.2 arcmin	–
5	671–1310	32.2–16.5 arcmin	–
6	1311–2300	16.5–9.4 arcmin	(a)
7	2301–5150	9.4–4.2 arcmin	(a)

Notes. (a) Not used in cosmological analysis. (b) No B-mode extracted.
The θ-ranges are just an indication and cannot be compared directly to θ-ranges used in real-space correlation function analyses due to the non-trivial functional dependence of these analyses on Bessel functions (cf. Section 5.7.1).

Table 5.2: Properties of the galaxy source sample.

redshift bin	z_{median}	N	n_{eff}	σ_e
z_1: $0.10 < z_{\mathrm{B}} \leq 0.45$	0.41	5 923 897	3.63 arcmin^{-2}	0.2895
z_2: $0.45 < z_{\mathrm{B}} \leq 0.90$	0.70	6 603 721	3.89 arcmin^{-2}	0.2848

Notes. The median redshift z_{median}, the total number of objects N, the effective number density of galaxies n_{eff} (cf. equation 5.17), and the dispersion of the intrinsic ellipticity distribution σ_e per redshift bin for the KiDS-450 dataset used in our analysis.

cosmological analysis we will drop the first and last band powers due to their potential noise-contamination which reduces the physical multipole range to $76 \leq \ell \leq 2300$. In addition to the E-modes we extract six B-mode band powers. Their multipole ranges coincide with the ranges of the E-mode bands 2–7 (due to the expected strong signal in the first E-mode band power a potential B-mode contamination is negligible). All ranges are summarized in Table 5.1 where we also indicate the corresponding angular scales. Note, however, that the naïve conversion from multipole to angular scales is insufficient for a proper comparison to correlation function results. An outline of how to compare both approaches properly is given in Section 5.7.1.

We calculate the effective number density of galaxies used in the lensing analysis following Heymans et al. (2012) as

$$n_{\mathrm{eff}} = \frac{1}{\Omega} \frac{\left(\sum_i w_i\right)^2}{\sum_i w_i^2} \,, \tag{5.17}$$

where w is the *lens*fit weight and the unmasked area is denoted as Ω. In Table 5.2 we list the effective number densities per KiDS patch and redshift bin. Note that there exist also alternative definitions for n_{eff} but the one used here has the practical advantage that it can be used directly to set the source number density in the creation of mock data.

In order to compare results later on to Hildebrandt et al. (2016) we only use sources in the range $0.10 < z_{\mathrm{B}} \leq 0.90$, where z_{B} is the Bayesian point estimate of the photometric redshifts.

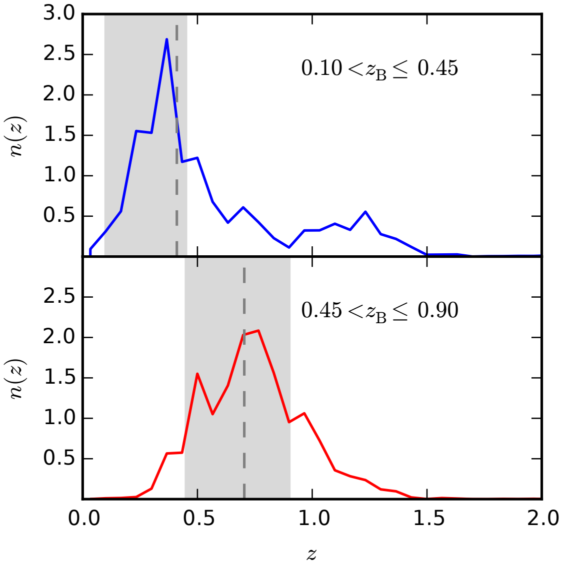

Figure 5.1: The normalized redshift distributions for the two tomographic bins employed in this study and estimated from the weighted direct calibration scheme ('DIR') presented in Hildebrandt et al. (2016). The dashed (grey) vertical lines mark the median redshift per bin (cf. Table 5.2) and the (grey) shaded regions indicate the target redshift selection by cutting on the Bayesian point estimate for photometric redshifts z_B.

We divide this range further into two broad tomographic bins z_1: $0.10 < z_B \leq 0.45$ and z_2: $0.45 < z_B \leq 0.90$ with similar effective number densities (cf. Table 5.2 and Fig. 5.1). Note that z_B is only used as a convenient quantity to define tomographic bins but does not enter anywhere else in the analysis. The limitation to only two redshift bins is due to run-time since the dimension of the fundamental covariance matrix (cf. equation 5.3) depends very strongly on the number of unique redshift correlations as noted already earlier.

5.5 Multiplicative bias correction and sensitivity to large-scale additive bias

The observed shear $\gamma_{\rm obs}$, measured as a weighted average of galaxy ellipticities, is generally a biased estimator of the true shear γ. The bias is commonly parametrized as (Heymans et al. 2006)

$$\gamma_{\rm obs} = (1 + m)\gamma + c \,, \tag{5.18}$$

where m and c refer to the multiplicative bias and additive bias, respectively.

The multiplicative bias is mainly caused by the effect of pixel noise in the measurements of galaxy ellipticities (Melchior & Viola 2012; Refregier et al. 2012; Miller et al. 2013), but it can also arise if the model used to describe the galaxy profile is incorrect, or if stars are misclassified as galaxies. The latter two effects are generally subdominant compared to the noise bias. We quantify the amplitude of the multiplicative bias in the KiDS data by means of a dedicated suite of image simulations (Fenech Conti et al. 2016). We closely follow the procedure described in Hildebrandt et al. (2016) and we derive a multiplicative correction for each tomographic bin, i.e. $m^{\rm fid}_{z_1} = -0.013 \pm 0.010$ and $m^{\rm fid}_{z_2} = -0.012 \pm 0.010$. The errorbars account both for statistical uncertainties and systematic errors due to small differences between data and simulations. In our likelihood analysis we apply the multiplicative correction to the measured shear power spectrum and in order to marginalize over the uncertainties on the m-correction we propagate them into the likelihood analysis. As the errors on the $m^{\rm fid}_{z_\mu}$ are fully correlated (Hildebrandt et al. 2016) we only need to include one free nuisance parameter. We vary $m_{\rm z_1}$ very conservatively within a 2σ tophat prior centred on its fiducial value in each step i of the likelihood estimation. The value for $m_{\rm z_2}$ is then fixed through the relation $m^i_{\rm z_2} = m^{\rm fid}_{\rm z_2} + \Delta m^i$ with $\Delta m^i = m^i_{z_1} - m^{\rm fid}_{z_1}$.

Additive biases are mainly caused by a residual PSF ellipticity in the shape of galaxies (e.g. Hoekstra 2004; van Uitert & Schneider 2016). More generally, any effect causing a preferential alignment of shapes in the galaxy source sample will create an additive bias. For example, in an early stage of the KiDS-450 data processing a small fraction of asteroids ended up in the galaxy source sample. This resulted in strongly aligned shape measurements with very high signal-to-noise causing a substantial c-term (cf. appendix D4 in Hildebrandt et al. 2016). This example also demonstrates that a potential c-term correction can only be derived empirically from the data: it is impossible to include every source for an additive bias in image simulations.

Here we demonstrate how the quadratic estimator can naturally deal with a residual additive shear in the data. This is a clear advantage over correlation function measurements, where the residual additive shear needs to be properly quantified and subtracted from the data, usually hampering the ability of measuring the cosmic shear signal at large angular separations.

If sufficiently low multipoles are included in the extraction of the first multipole band of the shear power spectrum band powers, this band accounts for any residual DC offset in the data such as the effect of a global c-term. For a clean demonstration of this feature, we employ Gaussian random fields (GRFs) with realistic CFHTLenS survey properties (e.g. masking, noise level; cf. **Chapter 4** for details). The GRFs were readily available and for this demonstration the differences in survey properties are negligible. We extract E- and B-modes simultaneously from four GRFs that match the W1, W2, W3, and W4 fields from CFHTLenS in size and shape. The measurements are performed in two broad redshift bins but we use the same multipole binning and shear pixel size $\sigma_{\rm pix}$ as used in the analysis of the KiDS-450 data (cf. Table 5.1). In a first step we extract a reference signal from the GRFs to which no additional global c-term was added. In a second step we apply a global additive term of $c = 2 \times 10^{-3}$ to both ellipticity components and re-extract the shear power spectra. In Fig. 5.2 we show the residuals between these two signals for all tomographic and multipole bins. As expected, only the first multipole bin is affected substantially by the global c-term, but all remaining bands are essentially unaffected. Hence, removing the first multipole bin from a subsequent cosmological analysis replaces a sophisticated global c-correction at reasonable computational costs.

5.6 Covariance

An important ingredient for an accurate and precise inference of cosmological parameters from the measured band powers is the covariance matrix. There are several approaches to estimate the covariance matrix: the brute-force approach of extracting it directly from a statistically significant number (to reduce numerical noise) of mock catalogues, an analytical calculation or, as a special feature of the quadratic estimator, the inverse of the Fisher matrix. Of course, each method has its specific advantages and disadvantages. The brute-force ap-

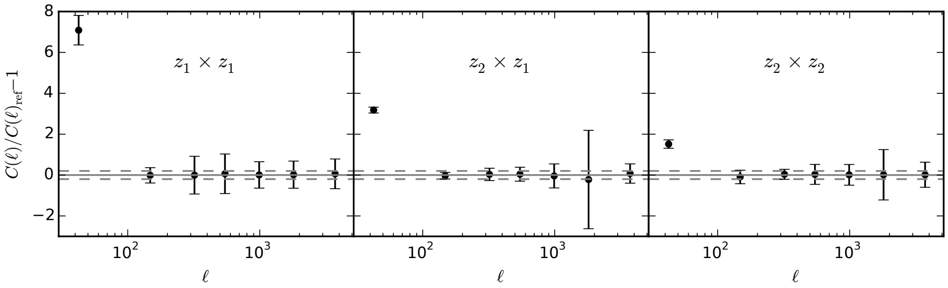

Figure 5.2: The residuals between a shear power spectrum extracted from reference Gaussian random fields (GRFs) and the one extracted from GRFs where a global c-term of $c = 2\times10^{-3}$ was applied to both ellipticity components. From left to right the unique correlations of the two redshift bins are shown. The GRFs were created to match the four fields of CFHTLenS in area, shape, noise properties, and redshift range (i.e. z_1: $0.50 < z_{\rm B} \leq 0.85$ and z_2: $0.85 < z_{\rm B} \leq 1.30$). The signal extraction, however, employs the multipole binning that is also used in the subsequent KiDS data analysis and extends to multipoles significantly below the one set by the field size. The globally applied c-term only affects the band power estimate of the first multipole bin but has no effect on the remaining bands. Hence, removing the first band power from a subsequent cosmological analysis is sufficient to account for a leftover global c-term in the data. The 1σ errorbars are based on the Fisher matrices and the horizontal dashed (grey) lines indicate ±20 per cent margins.

proach requires significant amounts of additional run-time, both for the creation of the mocks and the signal extraction. This can become a severe issue especially if the signal extraction is also computationally demanding, as is the case for the (tomographic) quadratic estimator. Moreover, if the mocks are based on N-body simulations the particle resolution and box size of these set fundamental limits for the scales that are available for a covariance estimation and to which level of accuracy and precision that is possible. In contrast, the Fisher matrix is computationally the cheapest estimate of a covariance matrix since it comes at no additional computational costs. However, it is only an accurate representation of the true covariance in the Gaussian limit and hence the errors for the non-linear scales will be underestimated. Moreover, the largest scale for a Fisher matrix based covariance is limited to the size of the patch. Therefore, the errors for scales corresponding to the patch size will also be underestimated. A possible solution to the shortcomings of the previous two approaches is the calculation of an analytical covariance matrix. This approach is computationally much less demanding than the brute-force approach and does not suffer from the scale-dependent limitations of the previous two approaches. Moreover, the non-Gaussian contributions at small scales can also be properly calculated. Hence, we follow the fiducial approach of Hildebrandt et al. (2016) and adopt their method for computing the analytical covariance (except for the final integration to correlation functions). The model for the analytical covariance consists of the following three components:

(i) a disconnected part that includes the Gaussian contribution to shape-noise, sample variance, and a mixed noise-sample variance term,

(ii) a non-Gaussian contribution from in-survey modes originating from the connected matter-trispectrum, and

(iii) a contribution from the coupling of in-survey and super-survey modes.

All cosmology dependent calculations employ a *WMAP9* cosmology (Hinshaw et al. 2013) and a detailed description of the full model will be presented in Joachimi et al. (in preparation).

We calculate the analytical covariance matrix $\mathbf{C}_{(\zeta\vartheta)(\gamma\phi)}(\ell, \ell')$ at integer multipoles ℓ, ℓ' over the range $10 \leq \ell, \ell' \leq 3000$[9] where the index pairs ζ, γ and ϑ, ϕ label the unique redshift correlations and band types (EE and BB), respectively. Note that the EE to BB and vice versa the BB to EE part of this matrix is zero, i.e. there is no power leakage for an ideal estimator. Finally, we create the analytical covariance matrix of the measured band powers by convolving $\mathbf{C}_{(\zeta\vartheta)(\gamma\phi)}(\ell, \ell')$ with the full band window matrix:

$$\mathbf{C}_{AB} = \widetilde{\mathbf{W}}_{A\zeta\vartheta}(\ell)\, \mathbf{C}_{(\zeta\vartheta)(\gamma\phi)}(\ell, \ell')\, (\widetilde{\mathbf{W}}^{\mathrm{T}})_{B\gamma\phi}(\ell') \,, \tag{5.19}$$

where the superindices A, B run over the band powers, their types (i.e. EE and BB), and the unique redshift correlations. $\widetilde{\mathbf{W}}$ is the band window matrix defined in equation (5.14) multiplied with the normalization for band powers, i.e. $\ell(\ell+1)/(2\pi)$. Note that the convolution with the band window matrix propagates all properties of the quadratic estimator into the band power covariance.

5.7 The KiDS-450 shear power spectrum

For each of the 13 subpatches of the five KiDS fields we extract the weak-lensing power spectrum in band powers spanning the multipole range $10 \leq \ell \leq 5150$ (cf. Section 5.4 and Table 5.1). The measurement is performed in two redshift bins in the ranges z_1: $0.10 < z \leq 0.45$ and z_2: $0.45 < z \leq 0.90$ (cf. Table 5.2). This yields in total two auto-correlation spectra and one unique cross-correlation spectrum per subpatch. In the subsequent analysis we combine all spectra by weighting each spectrum with the effective area of the subpatch. This weighting is optimal in the sense that the effective area is proportional to the number of galaxy pairs per patch and the number of pairs sets the shape-noise variance of the measurements. We present the resulting seven E-mode band powers in Fig. 5.3. The errors on the signal are estimated from the analytical covariance (cf. Section 5.6), which includes contributions from shape noise, cosmic variance, and super-sample variance. The extension along the multipole axis indicates the width of the band. The signal is plotted at the naïve centre of the band whereas for the subsequent likelihood analysis we take the window functions of the bands into account (cf. equation 5.13). Only the bands between the (grey) shaded areas enter in the cosmological analysis. We exclude the first band as it contains by construction multipoles that extend below the lowest physical multipole (i.e. $\ell_{\mathrm{field}} \approx 76$) in order to account for any remaining DC offset in the data (such as an additive global c-term, cf. Section 5.5). The last band at the highest multipoles is also excluded as it is designed to sum up the oscillating part of the pixel window function at high multipoles.

We simultaneously extract E- and B-modes. As noted in Section 5.2 the cosmological signal is contained entirely in the E-modes in the absence of systematics. Hence, the B-mode signal is used as a test for residual systematics in the data. We show the effective area weighted six B-mode band powers in Fig. 5.4. The B-mode errors are derived from the B-mode part of the inverse Fisher matrix as described in **Chapter 4**. We do not use the B-mode errors derived from the analytical covariance since they currently do not account for survey-boundary effects and therefore are underestimated.

In order to use the B-mode band powers as an independent test for residual systematics, we have to confirm that there is no significant leakage of power from E-modes to B-modes.

---

[9] This range is matching the range over which we later perform the summation when we convolve the theoretical signal predictions with the band window functions.

From a previous analysis (Lin et al. 2012) we do not expect the quadratic estimator to induce power leakage from E- to B-modes. However, if the shape noise is misestimated we might expect some power leakage for the highest multipole band powers. We investigate this using the band window functions derived from the full band window function matrix (cf. equation 5.14), which is also computed as an average over all subpatches with effective area weights. In Fig. 5.5 we show (red points) the convolution of a fiducial cosmological E-mode signal (employing the same *WMAP9* cosmology used for the calculation of the analytical covariance) for the low-redshift auto-correlation with the corresponding band window functions of all possible cross-terms (e.g. EE, $z_1 \times z_1$ to BB, $z_2 \times z_2$). The fiducial E-mode signal is plotted as the solid black line and the errorbars are derived from the analytical covariance. Additionally, we show a second set of errorbars in grey. These indicate the amplitude of the Fisher matrix based B-mode errors. We expect the signal to appear only in the leftmost panel depicting the auto-contribution (i.e. from EE, $z_1 \times z_1$ to EE, $z_1 \times z_1$). Indeed, the cross-term contributions are order(s) of magnitude lower than the E-mode band powers and well within the statistical B-mode errors. Hence, there is no significant power leakage from E- to B-modes which would introduce a detectable spurious B-mode signal.

Hence, the significance of the measured B-modes can now be used to assess whether or not there are residual systematics in the data. Qualitatively this is shown in Fig. 5.4. We test the hypothesis that the B-modes in the first five bands are consistent with zero by means of a χ^2-goodness-of-fit measure. This yields a reduced χ^2 of $\chi^2_{\mathrm{red}} = 1.06$ for 14 degrees of freedom. We conclude that the B-modes are consistent with zero over the multipole range used in the cosmological analysis.

In passing we note that Fig. 5.5 shows that the estimates of the fiducial E-mode power spectrum with the band window functions for bands 6 and 7 are biased low and high, respectively. This is visible in the auto-contribution (EE, $z_1 \times z_1$) to (EE, $z_1 \times z_1$), i.e. the leftmost panel. Therefore, we decide to conservatively remove band 6 from the subsequent cosmological analysis, which reduces the available multipole range to $76 \leq \ell \leq 1310$.

5.7.1 Qualitative comparison to correlation functions

Most cosmic shear studies to date employ real-space correlation functions (e.g. Heymans et al. 2013; Becker et al. 2015; Hildebrandt et al. 2016) because they are conceptually easy and fast to compute. In contrast to direct power spectrum estimates, correlation functions measured at a given angular separation sum up contributions over a wide range of multipoles. Due to this mode-mixing it is non-trivial to compare angular scales to multipole ranges, as well as to cleanly separate linear and non-linear scales.

As an example we qualitatively compare here correlation function measurements based on the angular scales presented in Hildebrandt et al. (2016) to the direct power spectrum measurements employing the quadratic estimator. For that purpose we calculate a fiducial shear power spectrum (cf. equation 5.5) employing a *Planck* cosmology (Planck Collaboration XIII 2015a) and the redshift distributions derived for our two tomographic bins. A correlation-function based estimator such as $\xi_\pm$ is related to the shear power spectrum $C_{\mu\nu}(\ell)$ through

$$\xi_\pm^{\mu,\nu}(\theta) = \frac{1}{2\pi} \int \mathrm{d}\ell \, \ell C_{\mu\nu}(\ell) J_{0,4}(\ell\theta) \equiv \int \mathrm{d}\ell \, I_{\xi_\pm}(\ell\theta) \,, \tag{5.20}$$

where θ is the angular distance between pairs of galaxies and $J_{0,4}$ is the zeroth- (for ξ_+) or fourth-order (for ξ_-) Bessel function of the first kind. In contrast, the quadratic estimator (QE) convolves the theoretical shear power spectrum with its band window matrix $W_A(\ell)$ (cf.

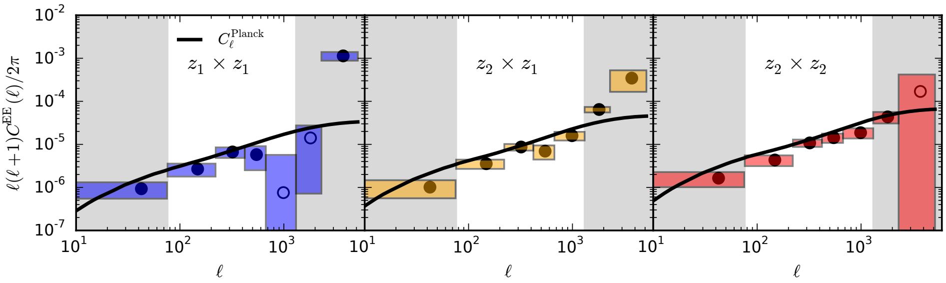

Figure 5.3: Measured E-mode band powers in tomographic bins averaged with the effective area per patch over all 13 KiDS-450 subpatches. From left to right we show the auto-correlation signal of the low-redshift bin (blue), the cross-correlation signal between the low and the high-redshift bin (orange), and the auto-correlation signal of the high-redshift bin (red). Note that negative band powers are shown at their absolute value with an open symbol. The low-redshift bin contains objects with redshifts in the range $0.10 < z_1 \leq 0.45$ and the high-redshift bin covers a range $0.45 < z_2 \leq 0.90$. The 1σ-errors in the signal are derived from the analytical covariance convolved with the averaged band window matrix (cf. Section 5.6) whereas the extension in ℓ-direction is the width of the band. Band powers in the shaded regions (grey) to the left and right of each panel are excluded from the cosmological analysis (see text for details). The solid line (black) shows the power spectrum for the cosmological model from (Planck Collaboration XIII 2015a). Note, however, that the band powers are centred at the naïve ℓ-bin centre and thus the convolution with the band window function is not taken into account in this plot, in contrast to the cosmological analysis.

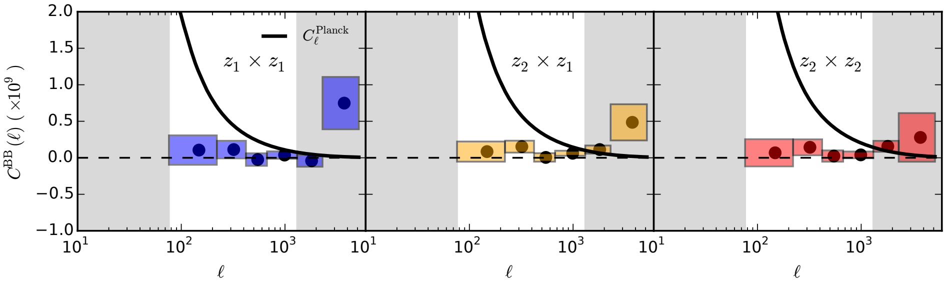

Figure 5.4: Same as Fig. 5.3 but for B-mode band powers. Note, however, the different scale (linear) and normalization used here with respect to Fig. 5.3; for reference we also plot a (Planck Collaboration XIII 2015a) based E-mode power spectrum as solid line (black). We show the measured B-modes as (black) dots with 1σ-errors derived from the averaged shape-noise contribution to the analytical covariance convolved with the B-mode part of the averaged band window matrix.

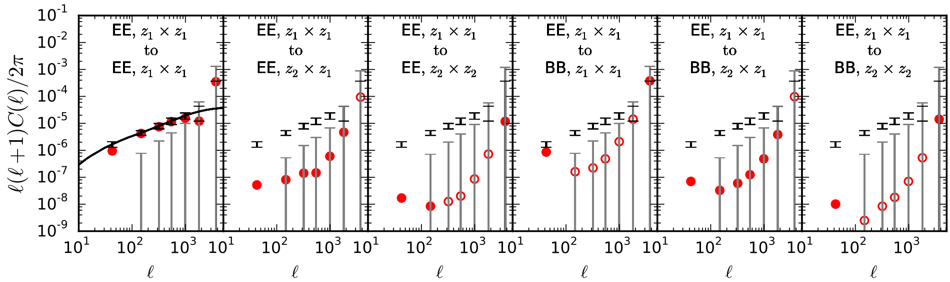

Figure 5.5: The contribution of a fiducial cosmological E-mode signal (solid, black line) for the low-redshift auto-correlation (i.e. $z_1 \times z_1$) convolved with the corresponding band window functions (red points) of all possible cross-combinations. The first panel from the left depicts the auto-contribution from (EE, $z_1 \times z_1$) to (EE, $z_1 \times z_1$). The grey errorbars show the statistical uncertainties associated with the B-modes. Open symbols denote negative values plotted at their absolute value. The corresponding plots for the remaining (EE, $z_2 \times z_1$) and (EE, $z_2 \times z_2$) cross-combinations are shown in Appendix 5.B.

equation 5.14):

$$\mathcal{B}_A = \sum_{\ell} \frac{\ell(\ell+1)}{2\pi} W_A(\ell) C_A(\ell) \equiv \sum_{\ell} I_{\mathrm{QE}}(\ell) \,, \tag{5.21}$$

where the superindex A runs again over all multipole bands and unique redshift correlations. The convolved power spectra as a function of multipoles defined at the right-hand sides of both equations are shown in Fig. 5.6 for the lowest redshift bin. In the upper panel we indicate the borders of the bands used in our cosmological analysis (grey dashed lines; cf. Table 5.1). In the two bottom panels we show the lower and upper limits of our power spectrum analysis. For the calculation of $I_{\xi_\pm}(\ell\theta)$ we use the central values of the $\theta_\pm$-intervals from the cosmic shear analysis of Hildebrandt et al. (2016). Fig. 5.6 shows that the ξ_+-measurements are highly correlated and anchored at very low multipoles, whereas the ξ_--measurements show a high degree of mode-mixing. In contrast, the quadratic estimator measurements of the power spectrum are much more cleanly separated and the degree of mode-mixing is much lower. We also note that correlation-function measurements get contributions from lower multipoles than $\ell < 76$ as well as multipoles larger than $\ell > 1310$, which in contrast do not contribute to the signal in our power spectrum analysis. Most of the cosmological information is contained in high multipoles and although the correlation-function measurements extend further into the high multipole regime, the contributions from these scales are non-negligible only for angular scales $\theta < 3\,\mathrm{arcmin}$. Hence, we do not expect significant differences in the precision of cosmological parameters between both approaches. However, the interpretation of the correlation-function signal at these scales requires accurate knowledge of the non-linear part of the matter power spectrum at high wavenumbers k.

5.8 Cosmological inference

The cosmological interpretation of the measured tomographic band powers $\mathcal{B}_\alpha$ derived in Section 5.7 is done in a Bayesian framework. For the estimation of cosmological parameters $\boldsymbol{p}$ we sample the shear likelihood

$$-2 \ln \mathcal{L}(\boldsymbol{p}) = \sum_{\alpha,\beta} d_\alpha(\boldsymbol{p}) (\mathbf{C}^{-1})_{\alpha\beta}\, d_\beta(\boldsymbol{p}) \,, \tag{5.22}$$

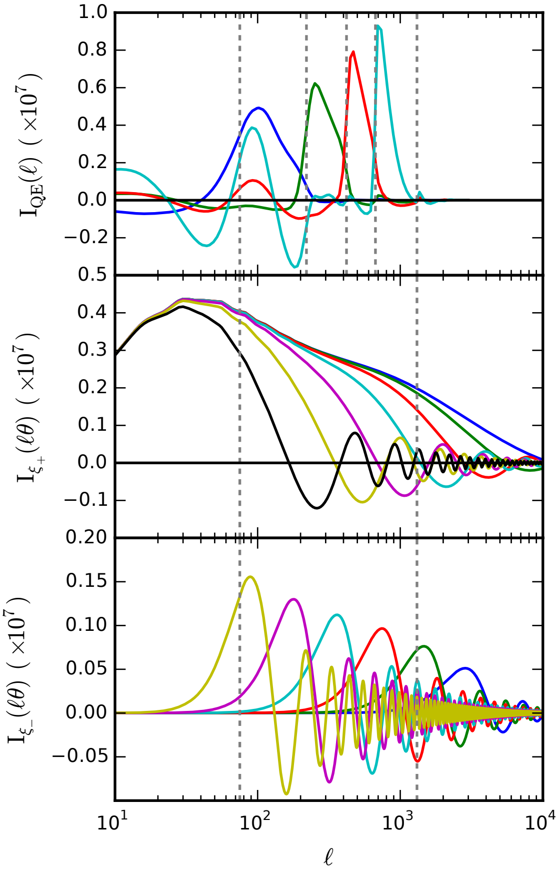

Figure 5.6: Top panel: measurement of a fiducial shear power spectrum using the quadratic estimator (cf. equation 5.21) in five band powers between $76 \leq \ell \leq 1310$. The borders of the bands are indicated by the vertical dashed (grey) lines. Mid panel: measurement of the same fiducial shear power spectrum using the ξ_+-statistics for correlation functions (cf. equation 5.20) in an angular range 0.7 arcmin $\leq \theta_+^{\rm cen} \leq 50$ arcmin. Bottom panel: measurements of the same fiducial shear power spectrum using the ξ_--statistics for correlation functions (cf. equation 5.20) in an angular range 6 arcmin $\leq \theta_-^{\rm cen} \leq 200$ arcmin.

where the indices α, β run over the tomographic bins. The covariance matrix $\mathbf{C}$ is the one calculated in Section 5.6 but employing only its E-mode part. The components of the data vector are calculated as

$$d_\alpha(\boldsymbol{p}) = (\mathcal{B}_\alpha - \langle \mathcal{B}_\alpha(\boldsymbol{p}) \rangle^{\text{model}}) \, , \tag{5.23}$$

where the dependence on cosmological parameters enters only in the calculation of the predicted E-mode band powers, $\langle \mathcal{B}^i(\ell) \rangle^{\text{model}}$ (cf. equations 5.13 and 5.5).

In addition to sampling the likelihood for the derivation of cosmological parameter constraints, we also intend to compare various model extensions to a baseline model in terms of the Bayes factor which is based on the evidences of the models. The Bayesian evidence $\mathcal{Z}$ is the normalization of the posterior over the parameters $\boldsymbol{p}$ (and usually ignored if one is only interested in parameter constraints). In that sense, however, it can also be interpreted as the average of the likelihood over the prior

$$\mathcal{Z} = \int \mathrm{d}^n \boldsymbol{p} \, \mathcal{L}(\boldsymbol{p}) \pi(\boldsymbol{p}) \, , \tag{5.24}$$

where $\pi(\boldsymbol{p})$ is the prior and n is the dimension of the parameter space. Hence, the Bayesian evidence naturally implements Occam's razor: a simpler theory with fewer parameters, i.e. a more compact parameter space, will result in a higher evidence compared to a theory that requires more parameters, unless the latter explains the data significantly better.

Based on the evidences for models M_1 and M_0 and the a priori probability ratio for the two models, $\mathrm{Pr}(M_1)/\mathrm{Pr}(M_0)$, the Bayes factor is defined as

$$K_{1,0} \equiv \frac{\mathcal{Z}_1}{\mathcal{Z}_0} \frac{\mathrm{Pr}(M_1)}{\mathrm{Pr}(M_0)} \, , \tag{5.25}$$

and can be used to make a decision between models M_1 and M_0 because $K_{1,0} > 1$ implies, for example, a preference of model M_1 over model M_0. Usually, $\mathrm{Pr}(M_1)/\mathrm{Pr}(M_0) = 1$ unless there are strong (physical) reasons to prefer one model over the other *a priori* which is not the case in our subsequent analysis. Furthermore, we will use the classification scheme of Kass & Raftery (1995) for the interpretation of the Bayes factor K (or equivalently $2 \ln K$).

For an efficient evaluation of the high-dimensional integral of equation (5.24) we employ the nested sampling algorithm MULTINEST[10] (Feroz & Hobson 2008; Feroz et al. 2009, 2013). Conveniently, its PYTHON-wrapper PYMULTINEST (Buchner et al. 2014) is included in the framework of the cosmological likelihood sampling package MONTE PYTHON[11] (Audren et al. 2013) with which we derive all cosmology-related results in this analysis.

5.8.1 Theoretical power spectrum

The calculation of the tomographic shear power spectrum $C_{\mu\nu}(\ell)$ is described in Section 5.2 and summarized by noting that it is just the projection of the 3D matter power spectrum P_δ along the line-of-sight weighted by lensing weight functions q_μ that take the lensing efficiency of each tomographic bin into account.

For the calculation of the matter power spectrum $P_\delta(k;\chi)$ in equation (5.5) we employ the Boltzmann-code CLASS[12] (Blas et al. 2011; Audren & Lesgourgues 2011). The non-linear corrections are implemented through the HALOFIT algorithm including the recalibration by Takahashi et al. (2012). Additionally, the effects of (massive) neutrinos are also implemented in

---

[10] Version 3.8 from `http://ccpforge.cse.rl.ac.uk/gf/project/multinest/`

[11] Version 2.2.1 from `https://github.com/baudren/montepython_public`

[12] Version 2.5.0 from `https://github.com/lesgourg/class_public`

CLASS following Lesgourgues & Tram (2011). Massive neutrinos introduce a redshift- and scale-dependent reduction of power in the matter power spectrum P_δ. However, this reduction of power also propagates into the lensing power spectra $C_{\mu\nu}(\ell)$, though smoothed by the lensing weight functions q_μ. In the multipole range considered in this analysis, we expect massive neutrinos to decrease the lensing power spectrum by an almost constant factor. Hence, the effect of massive neutrinos causes a degeneracy with cosmological parameters affecting the normalization of the lensing power spectrum.

In addition to massive neutrinos, the effect of baryon feedback is another source of a scale-dependent reduction of power, especially in the non-linear regime. Although the full physical description of baryon feedback is not established yet, hydrodynamical simulations offer one route to estimate its effect on the matter power spectrum. In general, the effect is quantified through a bias function with respect to the dark-matter only P_δ (e.g. Semboloni et al. 2013; Harnois-Déraps et al. 2015):

$$b^2(k, z) \equiv \frac{P_\delta^{\text{mod}}(k, z)}{P_\delta^{\text{ref}}(k, z)}\,, \tag{5.26}$$

where P_δ^{mod} and P_δ^{ref} denote the power spectra with and without baryon feedback, respectively.

In this work we make use of the results obtained from the OverWhelmingly Large Simulations (OWLS; Schaye et al. 2010, van Daalen et al. 2011) by implementing the fitting formula for baryon feedback derived in Harnois-Déraps et al. (2015):

$$b^2(k, z) = 1 - A_{\text{bary}}\left(A_z \mathrm{e}^{(B_z x - C_z)^3} - D_z x \mathrm{e}^{E_z x}\right), \tag{5.27}$$

where $x = \log_{10}(k/1\,\text{Mpc}^{-1})$ and the terms A_z, B_z, C_z, D_z, and E_z are functions of the scale factor $a = 1/(1 + z)$. These terms also depend on the baryonic feedback model and we refer the reader to Harnois-Déraps et al. (2015) for the specific functional forms and constants. Additionally, we introduce a general free amplitude A_{bary} which we will use as a free parameter to marginalize over while fitting for the cosmological parameters in some models.

We demonstrate the effects of massive neutrinos and baryon feedback on the 3D matter power spectrum and the shear power spectrum (employing the KiDS-450 lensing kernel of our analysis) in Fig. 5.7. Baryon feedback causes a significant reduction of power in the high multipole regime whereas massive neutrinos lower the amplitude of the shear power spectrum over all scales by an almost constant value.

In general, the observed shear power spectrum is a biased tracer of the cosmological convergence power spectrum due to the effect of intrinsic alignments (IA):

$$C_{\mu\nu}^{\text{tot}}(\ell) = C_{\mu\nu}^{\text{GG}}(\ell) + C_{\mu\nu}^{\text{II}}(\ell) + C_{\mu\nu}^{\text{GI}}(\ell)\,, \tag{5.28}$$

where C^{II} is the power spectrum of intrinsic ellipticity correlations between neighbouring galaxies (termed ‘II’) and C^{GI} is the power spectrum of correlations between the intrinsic ellipticities of foreground galaxies and the gravitational shear of background galaxies (termed ‘GI’). For the theoretical description of these effects we follow Hildebrandt et al. (2016) and employ the ‘linear non-linear’ model of intrinsic alignments (Hirata & Seljak 2004; Bridle & King 2007; Joachimi et al. 2011), so that we can write:

$$C_{\mu\nu}^{\text{II}}(\ell) = \int_0^{\chi_{\text{H}}} \mathrm{d}\chi\, \frac{n_\mu(\chi) n_\nu(\chi) F^2(\chi)}{f_{\text{K}}^2(\chi)} P_\delta\left(k = \frac{\ell}{f_{\text{K}}(\chi)}; \chi\right), \tag{5.29}$$

$$C_{\mu\nu}^{\text{GI}}(\ell) = \int_0^{\chi_{\text{H}}} \mathrm{d}\chi\, \frac{q_\nu(\chi) n_\mu(\chi) + q_\mu(\chi) n_\nu(\chi)}{f_{\text{K}}^2(\chi)} F(\chi) P_\delta\left(k = \frac{\ell}{f_{\text{K}}(\chi)}; \chi\right), \tag{5.30}$$

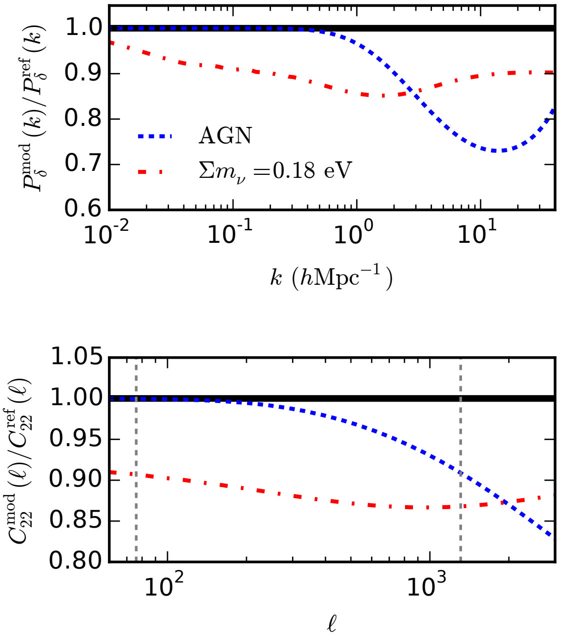

Figure 5.7: Upper panel: the ratio of modified matter power spectra over the dark matter only power spectrum. The dashed line (blue) shows the effect of the baryon feedback bias in the AGN model from OWLS (Schaye et al. 2010; van Daalen et al. 2011) using the implementation by Harnois-Déraps et al. (2015) (cf. equation 5.27 with $A_{\rm bary} = 1$). The modifications due to three degenerate massive neutrinos with total mass $\Sigma m_\nu = 0.18$ eV is demonstrated by the dash-dotted line (red). The redshift for the power spectrum calculation is $z = 0.7$ corresponding to the median redshift of the high-redshift bin used in the subsequent analysis (cf. Table 5.2). Lower panel: same as upper panel but for the lensing power spectrum of the high-redshift bin $z_2 : 0.45 < z_{\rm B} \leq 0.90$ (cf. Table 5.2). The vertical dashed (grey) lines mark the multipole range of the subsequent cosmological analysis (cf. Table 5.1).

with the lensing weight function $q_\mu(\chi)$ defined as in equation (5.6) and

$$F(\chi) = -A_{\rm IA} C_1 \rho_{\rm crit} \frac{\Omega_m}{D_+(\chi)} \, . \tag{5.31}$$

Here we also introduce a dimensionless amplitude $A_{\rm IA}$ which allows us to rescale and vary the fixed normalization $C_1 = 5 \times 10^{-14}\, h^{-2} {\rm M}_\odot{}^{-1} {\rm Mpc}^3$ in the subsequent likelihood analysis. The critical density of the Universe today is denoted as $\rho_{\rm crit}$ and $D_+(\chi)$ is the linear growth factor normalized to unity today. In general, equation (5.31) can include also a luminosity dependence and/or an additional redshift scaling. The majority of the KiDS-450 source sample consists of late-type galaxies for which no significant detection of intrinsic alignments exists to date. For massive early-type galaxies, however, a luminosity-dependent alignment signal has been measured with no indication for a redshift dependence (Joachimi et al. 2011; Singh et al. 2015). For their re-analysis of CFHTLenS, which is of similar statistical power as KiDS-450, Joudaki et al. (2016) concluded that the full flexibility of the intrinsic alignment model including either a luminosity dependence, or a redshift dependence, or both cannot be constrained sufficiently by the data. As a cross-check, we select galaxies between $20 < m_r < 24$ from COSMOS (Laigle et al. 2016) as a proxy for the KiDS sample and study their r-band luminosities. The ratio between the mean luminosities of the two tomographic bins used in this analysis is 1.03. Therefore, we can indeed neglect any luminosity dependence in the modelling of intrinsic alignments for our galaxy source sample. Hence, we follow Hildebrandt et al. (2016) and do not consider a luminosity dependence and/or additional redshift scaling. In order to facilitate the notation of equations (5.29) and (5.30) we have not introduced these additional terms in equation (5.31). Therefore, only a free amplitude $A_{\rm IA}$ is allowed for the modelling of intrinsic alignments in the subsequent likelihood analysis.

5.8.2 Models

The two most important parameters entering in the calculation of the shear power spectrum are $\Omega_{\rm m}$ the energy density of matter in the Universe today and $A_{\rm s}$ the amplitude of the primordial power spectrum. These two quantities determine the tilt and the total amplitude of the shear power spectrum, respectively. However, simultaneous changes in these two parameters have only a subtle net effect on the shear power spectrum and lead in general to a degeneracy in these two parameters. Moreover, observationally it is easier to work instead of $A_{\rm s}$ with the quantity σ_8 which is the root-mean-square variance of the density field smoothed with the Fourier transform of a tophat filter on a scale $R = 8\, h^{-1}{\rm Mpc}$ in real-space. Hence, the lensing-intrinsic degeneracy is usually referred to as a degeneracy in $\Omega_{\rm m}$ and σ_8 and the 2D projections of credibility intervals in this parameter plane define the lensing 'bananas'. The extent of these degeneracy 'bananas' (i.e. the top and bottom of the 'banana') is sensitive to the choice of sampling parameters (e.g. $A_{\rm s}$ or $\ln(10^{10} A_{\rm s})$) and their prior ranges. Moreover, a principal components analysis shows that the parameter combination $\sigma_8(\Omega_{\rm m}/0.3)^\alpha$, which essentially measures the width of the 'banana', is most robustly constrained by cosmic shear. In Fig. 5.8 we explicitly show this for two sets of priors as specified in Table 5.3. Increased priors for $\Omega_{\rm b} h^2$ and h have a significant impact on the extent of the 'banana' along the degeneracy line in the $\Omega_{\rm m}$–σ_8 plane as shown in Fig. 5.8. However, the increased prior ranges hardly influence the constraint on the parameter combination $\sigma_8(\Omega_{\rm m}/0.3)^\alpha$ for which we find $\sigma_8(\Omega_{\rm m}/0.3)^\alpha = 0.709 \pm 0.037$ for the fiducial prior ranges and $\sigma_8(\Omega_{\rm m}/0.3)^\alpha = 0.709 \pm 0.039$ for the increased prior ranges. Hence, we adopt the following strategy for the parameter sampling in this paper: we will sample in $\ln(10^{10} A_{\rm s})$ and $\Omega_{\rm cdm} h^2$ and treat σ_8 and $\Omega_{\rm m}$ as derived quantities in order to calculate the combined constraint $\sigma_8(\Omega_{\rm m}/0.3)^\alpha$. As opposed to previous analyses we refrain

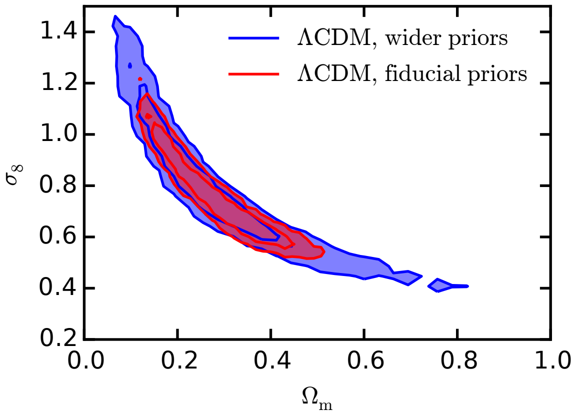

Figure 5.8: The 68 and 95 per cent credibility intervals in the Ω_m–σ_8 plane for the same baseline ΛCDM model employing two different sets of priors (cf. Table 5.3). The 'fiducial priors' (red contours) artificially cut the extent of the degeneracy 'banana' but leave its width unchanged in comparison to the 'wider priors' (blue contours). This results in consistent constraints on $\sigma_8(\Omega_\mathrm{m}/0.3)^\alpha$ yielding $\sigma_8(\Omega_\mathrm{m}/0.3)^\alpha = 0.709 \pm 0.037$ for the 'fiducial priors' $\sigma_8(\Omega_\mathrm{m}/0.3)^\alpha = 0.709 \pm 0.039$ for the 'wider priors'.

from showing any further 'banana'-plots due to their sensitivity to priors as shown in Fig. 5.8 in order to avoid any misleading interpretations (cf. the discussions of that in Joudaki et al. 2016; Hildebrandt et al. 2016).

In addition to the parameter combination $\sigma_8(\Omega_\mathrm{m}/0.3)^\alpha$ also the quantity $S_8 \equiv \sigma_8 \sqrt{\Omega_\mathrm{m}/0.3}$ is used in the literature based on the observation that the exponent α is usually found to be ≈ 0.5.

In the following likelihood analysis we assume a flat cosmological model and use the same set of parameters and priors from the analysis in Hildebrandt et al. (2016) for our fiducial model (referred to as 'ΛCDM' henceforth): $\Omega_\mathrm{cdm}h^2$, $\ln(10^{10}A_\mathrm{s})$, $\Omega_\mathrm{b}h^2$, n_s, h. The value of the Hubble parameter today is denoted as h, $\Omega_\mathrm{b}h^2$ is the baryonic matter density multiplied with h^2 and n_s is the exponent of the primordial power spectrum. Since data from particle physics experiments indicate that neutrinos have mass, we include two massless and one massive neutrino with a fixed minimal mass of $\Sigma m_\nu = 0.06\,\mathrm{eV}$. Moreover, we include a nuisance parameter m_{z_1} for the multiplicative correction in the first redshift bin and correlate the m-correction for the second redshift bin with it (cf. Section 5.4 for details). Since Hildebrandt et al. (2016) have shown that the uncertainty in the photometric redshift distribution is substantially smaller than the measurement errors and sampling variance on the cosmic shear signal, we do not include any nuisance parameter for the photometric redshift uncertainties. Having demonstrated the robustness of $\sigma_8(\Omega_\mathrm{m}/0.3)^\alpha$ and S_8 under a change of priors and in the interest of run-time we choose to employ narrow priors on h and $\Omega_\mathrm{b}h^2$. The prior range on h corresponds to the $\pm 5\sigma$ uncertainty centred on the distance-ladder constraint from Riess et al. (2016) of $h = 0.730 \pm 0.018$. Note that the corresponding prior range of $0.64 < h < 0.82$ still includes the preferred value from Planck Collaboration XIII (2015a). The prior on $\Omega_\mathrm{b}h^2$ is based on BBN constraints listed in the 2015 update from the Particle Data Group (Olive & Particle Data Group 2014) again adopting a conservative width of $\pm 5\sigma$ such that $0.019 < \Omega_\mathrm{b}h^2 < 0.026$.

Since we also want to constrain the total mass of massive neutrinos, we introduce as the

Table 5.3: Set of priors used for Fig. 5.8.

Parameter	fiducial priors	wider priors
$\Omega_{\mathrm{cdm}}h^2$	$[0.01, 0.99]$	$[0.01, 0.99]$
$\ln(10^{10}A_{\mathrm{s}})$	$[1.7, 5.]$	$[1.7, 5.]$
$\Omega_{\mathrm{b}}h^2$	$[0.019, 0.026]$	$[0.001, 0.010]$
n_{s}	$[0.7, 1.3]$	$[0.7, 1.3]$
h	$[0.64, 0.82]$	$[0.3, 1.]$
Σm_ν (eV)	$\equiv 0.06$	$\equiv 0.06$
m_{z_1}	$[-0.033, 0.007]$	$[-0.033, 0.007]$
Ω_{m}	derived	derived
σ_8	derived	derived

Notes. The primary cosmological and nuisance parameters for the baseline ΛCDM model for two sets of prior ranges used for Fig. 5.8. The 'fiducial priors' are used in the subsequent cosmological analysis.

first model extension the free parameter Σm_ν (the model is referred to as 'ΛCDM+Σm_ν'). However, as we have discussed in Section 5.8.1 there are other physical effects that we need to take into account because they might create degenerate signatures in the matter and/or shear power spectra. The first of such physical parameters is the amplitude for the intrinsic alignment model, i.e. A_{IA}. We refer to this model subsequently as 'ΛCDM+A_{IA}'. The second physical nuisance is baryon feedback and hence the model 'ΛCDM+A_{bary}' includes the free amplitude A_{bary}. We combine both physical nuisance effects and study their combined impact on cosmological constraints in the model 'ΛCDM+A_{IA}+A_{bary}'. Finally, we combine all previous extensions into one model which we dub 'ΛCDM+all' for brevity instead of showing all extensions explicitly, i.e. A_{IA}, A_{bary}, and Σm_ν.

5.8.3 Results and discussion

The resulting cosmological parameter constraints for all models and the corresponding prior ranges are summarized in Table 5.4. In order to highlight parameter degeneracies we show all possible 2D parameter projections in Fig. 5.10 in Appendix 5.B for the model ΛCDM+all. This model can be considered as the most conservative one as it includes marginalizations over several nuisance parameters (cf Section 5.8.2). For this model we derive an upper bound on the total mass for three degenerate massive neutrinos. We find $\Sigma m_\nu < 3.46\,\mathrm{eV}$ at 95 per cent credibility from lensing alone. This is very similar to the constraint from our previous CFHTLenS re-analysis in **Chapter 4**. In contrast, the upper bound at 95 per cent confidence found by Planck Collaboration XIII (2015a, TT+lowP) is $\Sigma m_\nu < 0.72\,\mathrm{eV}$. Combining the *Planck* CMB results with measurements of the Ly α power spectrum and BAO measurements yields the very stringent upper limit of $\Sigma m_\nu < 0.14\,\mathrm{eV}$ at 95 per cent confidence (Palanque-Delabrouille et al. 2015).

Table 5.4: Cosmological parameter constraints.

Model	$\Omega_{\rm cdm}h^2$	$\ln(10^{10}A_{\rm s})$	$\Omega_{\rm m}$	σ_8	$\Omega_{\rm b}h^2$	$n_{\rm s}$	h	Σm_ν (eV)	m_{z_1}	$A_{\rm IA}$	$A_{\rm bary}$
Prior ranges	$[0.01, 0.99]$	$[1.7, 5.]$	derived	derived	$[0.019, 0.026]$	$[0.7, 1.3]$	$[0.64, 0.82]$	$[0.06, 10.]$	$[-0.033, 0.007]$	$[-6., 6.]$	$[0., 10.]$
ΛCDM no sys.	$0.13^{+0.06}_{-0.08}$	$2.60^{+0.78}_{-0.90}$	$0.29^{+0.10}_{-0.14}$	$0.72^{+0.19}_{-0.17}$	$0.022^{+0.004}_{-0.004}$	$0.93^{+0.16}_{-0.22}$	$0.74^{+0.08}_{-0.06}$	$\equiv 0.06$	–	–	–
ΛCDM	$0.14^{+0.06}_{-0.07}$	$2.61^{+0.84}_{-0.91}$	$0.29^{+0.09}_{-0.14}$	$0.72^{+0.12}_{-0.17}$	$0.023^{+0.004}_{-0.003}$	$0.93^{+0.12}_{-0.20}$	$0.74^{+0.08}_{-0.09}$	$\equiv 0.06$	$-0.007^{+0.014}_{-0.009}$	–	–
ΛCDM+Σm_ν	$0.17^{+0.06}_{-0.09}$	$2.53^{+0.63}_{-0.83}$	$0.37^{+0.13}_{-0.11}$	$0.62^{+0.08}_{-0.11}$	$0.022^{+0.003}_{-0.004}$	$1.05^{+0.24}_{-0.16}$	$0.76^{+0.06}_{-0.05}$	$1.67^{+0.73}_{-1.61}$	$-0.008^{+0.015}_{-0.013}$	–	–
ΛCDM+$A_{\rm IA}$	$0.12^{+0.05}_{-0.07}$	$2.73^{+1.10}_{-1.03}$	$0.27^{+0.09}_{-0.12}$	$0.74^{+0.16}_{-0.18}$	$0.023^{+0.004}_{-0.003}$	$0.95^{+0.16}_{-0.19}$	$0.74^{+0.08}_{-0.07}$	$\equiv 0.06$	$-0.007^{+0.014}_{-0.010}$	$-0.22^{+1.63}_{-1.34}$	–
ΛCDM+$A_{\rm bary}$	$0.12^{+0.06}_{-0.07}$	$2.80^{+1.01}_{-1.10}$	$0.27^{+0.07}_{-0.12}$	$0.79^{+0.14}_{-0.20}$	$0.022^{+0.003}_{-0.003}$	$1.09^{+0.21}_{-0.13}$	$0.74^{+0.08}_{-0.07}$	$\equiv 0.06$	$-0.008^{+0.015}_{-0.009}$	–	$3.85^{+1.90}_{-2.94}$
ΛCDM+$A_{\rm IA}$+$A_{\rm bary}$	$0.12^{+0.05}_{-0.06}$	$2.91^{+1.27}_{-1.21}$	$0.26^{+0.08}_{-0.11}$	$0.80^{+0.18}_{-0.20}$	$0.023^{+0.003}_{-0.003}$	$1.10^{+0.20}_{-0.11}$	$0.74^{+0.08}_{-0.05}$	$\equiv 0.06$	$-0.007^{+0.014}_{-0.007}$	$-0.34^{+1.51}_{-1.33}$	$4.03^{+2.31}_{-2.73}$
ΛCDM+all	$0.14^{+0.05}_{-0.07}$	$2.82^{+1.03}_{-1.12}$	$0.32^{+0.09}_{-0.12}$	$0.69^{+0.10}_{-0.15}$	$0.022^{+0.003}_{-0.003}$	$1.13^{+0.17}_{-0.13}$	$0.75^{+0.07}_{-0.05}$	$1.16^{+0.54}_{-1.10}$	$-0.007^{+0.014}_{-0.011}$	$-0.32^{+1.43}_{-1.23}$	$3.15^{+1.81}_{-3.15}$

Notes. We quote weighted median values for each varied parameter and derive 1σ-errors using the 68 per cent credible interval of the marginalized posterior distribution.

The cosmological main results for each model, i.e. $\sigma_8(\Omega_\mathrm{m}/0.3)^\alpha$ and S_8, are summarized in Table 5.5. We derive the exponent α from fitting the function $\ln\sigma_8(\Omega_\mathrm{m}) = -\alpha\ln\Omega_\mathrm{m} + \mathrm{const.}$ to the likelihood surface in the Ω_m–σ_8 plane. Since indeed $\alpha \approx 0.5$ for all models, we compare their S_8 values in Fig. 5.9 to each other but also to constraints from other cosmic shear analyses and CMB constraints. The values we derive for each of the models in this analysis are consistent with each other and as expected introducing a free total neutrino mass is shifting S_8 to lower values. Most of our models are also consistent with previous results from CFHTLenS, where we compare in particular to a correlation-function re-analysis employing six tomographic bins and marginalization over various nuisance parameters from Joudaki et al. (2016). In addition to that, we show results from our previous quadratic estimator analysis of CFHTLenS from **Chapter 4**, which employed two tomographic bins at higher redshift compared to the bins used here. In that study the basic five-parameter model was also labelled 'ΛCDM' but did not include a marginalization over the shear calibration uncertainties. The label 'ΛCDM+all' used in that study also refers to an extension of the 'ΛCDM' model with a free total neutrino mass and marginalization over baryon feedback, but does not take intrinsic alignments into account. The errors are comparable to the errors in this study, since CFHTLenS and KiDS-450 have comparable statistical power. The comparison to the KiDS-450 constraint from the correlation-function analysis with four tomographic bins (Hildebrandt et al. 2016) shows that the errorbars of that study are about 32 per cent smaller than the ones derived here. Following the discussion of Section 5.7.1 we attribute this mainly to the increased resolution along the line-of-sight for four tomographic bins, which improves the precision on the intrinsic alignment modelling. A small increase in the errorbars might also be explained by the multipole range used in this analysis compared to the effective multipole range used in Hildebrandt et al. (2016). Our results are also consistent with the result from the DES science verification (SV) correlation-function analysis (DES Collaboration 2015, 'Fiducial DES SV cosmic shear').

More interesting is the comparison of our results to CMB constraints including pre-*Planck* (Hinshaw et al. 2013; Calabrese et al. 2013) and *Planck* (Planck Collaboration XIII 2015a; Spergel et al. 2015) data. We find them to be most distinctively in tension with the results from Planck Collaboration XIII (2015a) at 1.8σ. We remind the reader to be cautious when quantifying tension between datasets based on parameter projections of the multi-dimensional likelihoods (cf. appendix A in MacCrann et al. 2015) which, for example, suffices to explain the mild tension in S_8 between our previous CFHTLenS results and *Planck*. However, this projection effect can certainly not explain the current tension in S_8 with *Planck*.

Finally, we want to decide which of our tested models fits the data the best. As indicated in Section 5.8 we employ for that a Bayesian model comparison framework based on evidences, their ratios, and the quantitative interpretation scheme of these by Kass & Raftery (1995). The results for the comparison of all model extensions to the baseline ΛCDM model are summarized in Table 5.6. In conclusion, none of the model extensions yields any positive evidence against the baseline ΛCDM model. Only adding a baryon feedback amplitude A_bary yields evidence 'not worth more than a bare mention' against the baseline ΛCDM model.

5.9 Conclusions

In this study we applied the quadratic estimator to state-of-the-art shear data from KiDS-450 in two redshift bins over the range $0.10 < z_\mathrm{B} \leq 0.90$ and extracted the band powers of the auto-correlation and cross-correlation shear power spectra for multipoles in the range $76 \leq \ell \leq 1310$. The covariance matrix is based on an analytical calculation which is then convolved with the full band window matrix. We derive the parameter combination $S_8 \equiv$

Table 5.5: Constraints on S_8 and $\sigma_8(\Omega_\mathrm{m}/0.3)^\alpha$.

Model	$S_8 \equiv \sigma_8\sqrt{\Omega_\mathrm{m}/0.3}$	Mean error on S_8	$\sigma_8 (\Omega_\mathrm{m}/0.3)^\alpha$	α
ΛCDM no sys.	$0.707^{+0.041}_{-0.036}$	0.038	$0.704^{+0.038}_{-0.034}$	0.544
ΛCDM	$0.712^{+0.039}_{-0.038}$	0.039	$0.709^{+0.038}_{-0.036}$	0.543
ΛCDM+Σm_ν	$0.696^{+0.040}_{-0.036}$	0.038	$0.692^{+0.039}_{-0.036}$	0.468
ΛCDM+A_IA	$0.703^{+0.053}_{-0.044}$	0.048	$0.699^{+0.051}_{-0.043}$	0.542
ΛCDM+A_bary	$0.754^{+0.047}_{-0.050}$	0.048	$0.747^{+0.044}_{-0.045}$	0.563
ΛCDM+A_IA+A_bary	$0.742^{+0.057}_{-0.056}$	0.057	$0.734^{+0.057}_{-0.050}$	0.555
ΛCDM+all	$0.710^{+0.053}_{-0.051}$	0.052	$0.710^{+0.053}_{-0.051}$	0.501

Notes. We quote weighted mean values for the constraints on $S_8 \equiv \sigma_8\sqrt{\Omega_\mathrm{m}/0.3}$ and $\sigma_8(\Omega_\mathrm{m}/0.3)^\alpha$. The errors denote the 68 per cent credible interval derived from the marginalized posterior distribution.

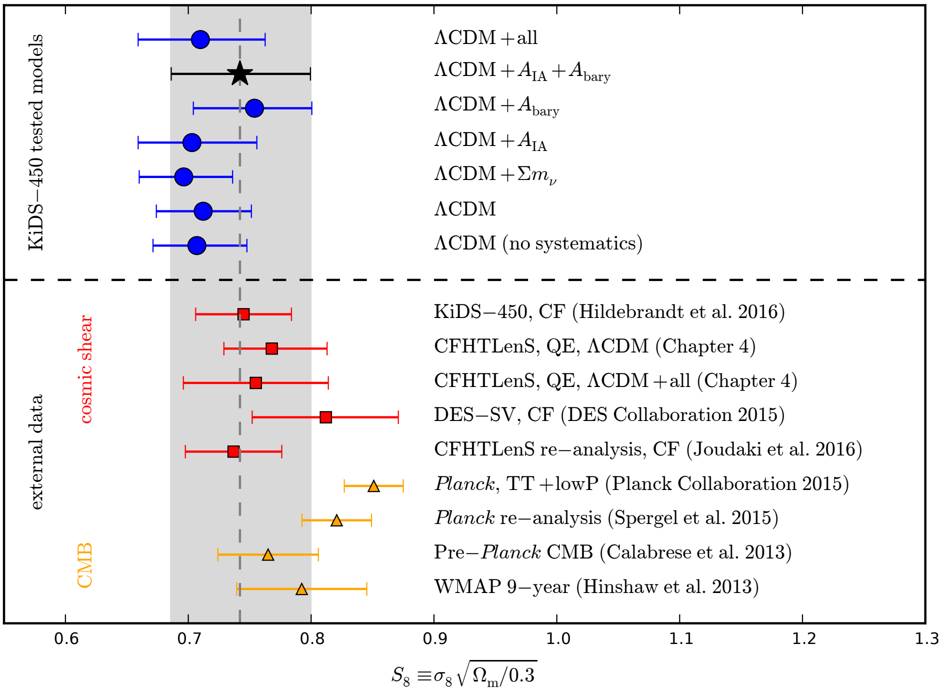

Figure 5.9: The 1σ-constraints on the parameter combination $S_8 \equiv \sigma_8\sqrt{\Omega_\mathrm{m}/0.3}$ for all of our tested models (cf. Tables 5.4 and 5.5). We compare them to constraints from other cosmic shear and CMB analyses. For cosmic shear analyses we indicate the type of estimator used with ‘CF’ for correlation functions and ‘QE’ for the quadratic estimator.

Table 5.6: Evidences from likelihood sampling.

Model	$\ln \mathcal{Z}$	$2 \ln K$ ($K \equiv \mathcal{Z}_i / \mathcal{Z}_{\Lambda\mathrm{CDM}}$)	Evidence against ΛCDM
ΛCDM no sys.	-10.43 ± 0.06	–	–
ΛCDM	-10.77 ± 0.06	0	–
ΛCDM+Σm_ν	-11.24 ± 0.06	-0.94	–
ΛCDM+A_{IA}	-11.80 ± 0.06	-2.06	–
ΛCDM+A_{bary}	-10.74 ± 0.06	0.06	'not worth more than a bare mention'
ΛCDM+A_{IA}+A_{bary}	-11.76 ± 0.06	-1.98	–
ΛCDM+all	-12.74 ± 0.07	-3.94	–

Notes. For each model we calculate the global log-evidence, $\ln \mathcal{Z}$, and compare all evidences in terms of the Bayes factor K (or equivalently $2 \ln K$) to the baseline ΛCDM model. The interpretation of the Bayes factor is following the scheme proposed by Kass & Raftery (1995).

$\sigma_8 \sqrt{\Omega_{\mathrm{m}}/0.3}$ for a baseline ΛCDM model and several model extensions including a free total mass of neutrinos and physical nuisances such as intrinsic alignments and baryon feedback. All models also include a marginalization over the small uncertainties of the shear calibration.

A Bayesian model comparison yields no evidence against the baseline ΛCDM model for any of the extensions introduced here including a free total mass for three degenerate massive neutrinos (Σm_ν) or physical nuisances such as baryon feedback (A_{bary}) or intrinsic alignments (A_{IA}). We take the conservative approach of considering the extended model ΛCDM+A_{IA}+A_{bary} as our fiducial model for which we find $S_8 = 0.742 \pm 0.057$. The flat five-parameter ΛCDM model without any systematics yields $S_8 = 0.707 \pm 0.038$. Thus, marginalizing over the shear calibration and the physical nuisance parameters increases the errorbars by ≈50 per cent.

For the model ΛCDM+all we derive an upper limit on the total mass of three degenerate neutrinos: $\Sigma m_\nu < 3.46\,\mathrm{eV}$ at 95 per cent credibility from lensing alone. This constraint is currently not competitive with respect to constraints derived from CMB or other large-scale structure measurements or the combination of both, but it is consistent with the constraint we derived already in our re-analysis of CFHTLenS whose statistical power is comparable to this analysis.

Most interestingly, the constraint on S_8 is in tension with the constraint from *Planck* at 1.8σ. This confirms the result from a 4-bin tomographic correlation-function analysis by Hildebrandt et al. (2016) with lower significance though due to the weaker S_8 constraint of our study. Moreover, the fact that this study uses less of the very non-linear scales in comparison to Hildebrandt et al. (2016) also disfavours insufficient modelling of these scales as a possible explanation for the discrepancy with *Planck*.

Acknowledgements

FK acknowledges support from a de Sitter Fellowship of the Netherlands Organization for Scientific Research (NWO) under grant number 022.003.013.

Based on data products from observations made with ESO Telescopes at the La Silla Paranal Observatory under programme IDs 177.A-3016, 177.A-3017 and 177.A-3018, and on data products produced by Target/OmegaCEN, INAF-OACN, INAF-OAPD and the KiDS production team, on behalf of the KiDS consortium. OmegaCEN and the KiDS production team acknowledge support by NOVA and NWO-M grants. Members of INAF-OAPD and INAF-

OACN also acknowledge the support from the Department of Physics & Astronomy of the University of Padova, and of the Department of Physics of Univ. Federico II (Naples).

Bibliography

Addison G. E., Huang Y., Watts D. J., Bennett C. L., Halpern M., Hinshaw G., Weiland J. L., 2016, ApJ, 818, 132

Audren B., Lesgourgues J., 2011, J. Cosmology Astropart. Phys., 2011, 037

Audren B., Lesgourgues J., Benabed K., Prunet S., 2013, J. Cosmology Astropart. Phys., 2013, 001

BOSS Collaboration, 2015, Phys. Rev. D, 92, 123516

Bartelmann M., Schneider P., 2001, Phys. Rep., 340, 291

Becker M. R., et al., 2015, preprint (arXiv:1507.05598)

Begeman K., Belikov A. N., Boxhoorn D. R., Valentijn E. A., 2013, Exp. Astron., 35, 1

Benítez N., 2000, ApJ, 536, 571

Benjamin J., et al., 2013, MNRAS, 431, 1547

Beutler F., et al., 2014, MNRAS, 443, 1065

Blas D., Lesgourgues J., Tram T., 2011, J. Cosmology Astropart. Phys., 2011, 034

Bond J. R., Jaffe A. H., Knox L., 1998, Phys. Rev. D, 57, 2117

Bridle S., King L., 2007, New J. Phys., 9, 444

Brown M. L., Taylor A. N., Bacon D. J., Gray M. E., Dye S., Meisenheimer K., Wolf C., 2003, MNRAS, 341, 100

Buchner J., et al., 2014, A&A, 564, A125

Calabrese E., et al., 2013, Phys. Rev. D, 87, 103012

Choi A., et al., 2015, preprint (arXiv:1512.03626)

DES Collaboration, 2015, preprint (arXiv:1507.05552)

Di Valentino E., Melchiorri A., Silk J., 2015, Phys. Rev. D, 92, 121302

Driver S. P., et al., 2011, MNRAS, 413, 971

Erben T., et al., 2005, Astron. Nachr., 326, 432

Erben T., et al., 2009, A&A, 493, 1197

Erben T., et al., 2013, MNRAS, 433, 2545

Fenech Conti I., Herbonnet R., Hoekstra H., Merten J., Miller L., Viola M., 2016, preprint (arXiv:1606.05337)

Feroz F., Hobson M. P., 2008, MNRAS, 384, 449

Feroz F., Hobson M. P., Bridges M., 2009, MNRAS, 398, 1601

Feroz F., Hobson M. P., Cameron E., Pettitt A. N., 2013, preprint (arXiv:1306.2144)

Fields B. D., Olive K. A., 2006, Nuclear Physics A, 777, 208

Gil-Marín H., Percival W. J., Verde L., Brownstein J. R., Chuang C.-H., Kitaura F.-S., Rodríguez-Torres S. A., Olmstead M. D., 2016, preprints (arXiv:1606.00439)

Harnois-Déraps J., Waerbeke L. v., Viola M., Heymans C., 2015, MNRAS, 450, 1212

Heymans C., et al., 2005, MNRAS, 361, 160

Heymans C., et al., 2006, MNRAS, 368, 1323

Heymans C., et al., 2012, MNRAS, 427, 146

Heymans C., et al., 2013, MNRAS, 432, 2433

Hikage C., Takada M., Hamana T., Spergel D., 2011, MNRAS, 412, 65

Hildebrandt H., et al., 2012, MNRAS, 421, 2355

Hildebrandt H., et al., 2016, preprint (arXiv:1606.05338)

Hinshaw G., et al., 2013, ApJS, 208, 19

Hirata C. M., Seljak U., 2004, Phys. Rev. D, 70, 063526

Hoekstra H., 2004, MNRAS, 347, 1337

Hu W., White M., 2001, ApJ, 554, 67

Ivezic Z., et al., 2008, preprint (arXiv:0805.2366)

Jarvis M., et al., 2015, preprint (arXiv:1507.05603)

Joachimi B., Mandelbaum R., Abdalla F. B., Bridle S. L., 2011, A&A, 527, 26

Joudaki S., et al., 2016, preprint (arXiv:1601.05786)

Kass R. E., Raftery A. E., 1995, J. Am. Stat. Assoc., 90, 773

Kilbinger M., 2015, Rep. Prog. Phys., 78, 086901

Kitching T. D., et al., 2014, MNRAS, 442, 1326

Knox L., 1999, Phys. Rev. D, 60, 103

Kuijken K., et al., 2015, MNRAS, 454, 3500

Laigle C., et al., 2016, ApJS, 224, 24

Laureijs R., et al., 2011, preprint (arXiv:1110.3193),

Lesgourgues J., Pastor S., 2006, Phys. Rep., 429, 307

Lesgourgues J., Tram T., 2011, J. Cosmology Astropart. Phys., 2011, 032

Lima M., Cunha C. E., Oyaizu H., Frieman J., Lin H., Sheldon E. S., 2008, MNRAS, 390, 118

Limber D. N., 1954, ApJ, 119, 655

Lin H., et al., 2012, ApJ, 761, 15

MacCrann N., Zuntz J., Bridle S., Jain B., Becker M. R., 2015, MNRAS, 451, 2877

Melchior P., Viola M., 2012, MNRAS, 424, 2757

Miller L., et al., 2013, MNRAS, 429, 2858

Newman J. A., et al., 2015, Astropart. Phys., 63, 81

Olive K. A., Particle Data Group 2014, Chinese Physics C, 38, 090001

Palanque-Delabrouille N., et al., 2015, J. Cosmology Astropart. Phys., 2015, 045

Planck Collaboration XIII, 2015a, preprint (arXiv:1502.01589)

Planck Collaboration XXIV, 2015b, preprint (arXiv:1502.01597)

Refregier A., Kacprzak T., Amara A., Bridle S., Rowe B., 2012, MNRAS, 425, 1951

Riess A. G., et al., 2016, preprint (arXiv:1604.01424)

SNO Collaboration, 2001, Phys. Rev. Lett., 87, 071301

SNO Collaboration, 2002, Phys. Rev. Lett., 89, 011301

Samushia L., et al., 2014, MNRAS, 439, 3504

Schaye J., et al., 2010, MNRAS, 402, 1536

Schirmer M., 2013, ApJS, 209, 21

Seljak U., 1998, ApJ, 506, 64

Semboloni E., Hoekstra H., Schaye J., van Daalen M. P., McCarthy I. G., 2011, MNRAS, 417, 2020

Semboloni E., Hoekstra H., Schaye J., 2013, MNRAS, 434, 148

Singh S., Mandelbaum R., More S., 2015, MNRAS, 450, 2195

Spergel D. N., Flauger R., Hložek R., 2015, Phys. Rev. D, 91, 023518

Super-Kamiokande Collaboration, 1998, Phys. Rev. Lett., 81, 1562

Takahashi R., Sato M., Nishimichi T., Taruya A., Oguri M., 2012, ApJ, 761, 152

Valentijn E. A., et al., 2007. eprint: arXiv:astro-ph/0702189, p. 491, `http://adsabs.harvard.edu/abs/2007ASPC..376..491V`

de Haan T., et al., 2016, preprints (arXiv:1603.06522)

de Jong J. T. A., Verdoes Kleijn G. A., Kuijken K. H., Valentijn E. A., 2013, Exp. Astron., 35, 25 de Jong J. T. A., et al., 2015, A&A, 582, A62

van Daalen M. P., Schaye J., Booth C. M., Dalla Vecchia C., 2011, MNRAS, 415, 3649

van Uitert E., Schneider P., 2016, preprint (arXiv:1605.01056)

5.A Updated derivation of the window function matrix

The full index notation for all matrices and tensors used in the quadratic estimator algorithm can be found in Appendix 4.A. Here, we only update the notation for the derivatives of the full covariance matrix $\mathbf{C}$ with respect to the power at an integer multipole ℓ, i.e. $\mathbf{D}_{\zeta\vartheta}(\ell)$. These are required for the calculation of the window function matrix (cf. equation 5.14) and enter explicitly in the computation of the trace matrix $\mathbf{T}$ (cf. equation 5.15):

$$\begin{aligned}\frac{\partial C_{(\mu\nu)(ab)(ij)}}{\partial \mathcal{B}_{\zeta\vartheta}(\ell)} &= \frac{M_{\zeta(\mu\nu)}}{2(\ell+1)}\left[w_0(\ell) I^{\vartheta}_{(ab)(ij)} + \tfrac{1}{2}\, w_4(\ell) Q^{\vartheta}_{(ab)(ij)}\right] \\ &\equiv D_{(\mu\nu)(ab)(ij)(\zeta)(\vartheta)}(\ell) \equiv \mathbf{D}_{\zeta\vartheta}(\ell)\,,\end{aligned} \tag{5.32}$$

where we have used that

$$C^{\mathrm{sig}}_{(\mu\nu)(ab)(ij)} = \sum_{\zeta,\vartheta,\ell} \mathcal{B}_{\zeta\vartheta}(\ell) \frac{M_{\zeta(\mu\nu)}}{2(\ell+1)} [w_0(\ell) I^{\vartheta}_{(ab)(ij)} + \tfrac{1}{2}\, w_4(\ell) Q^{\vartheta}_{(ab)(ij)}]\ .$$

5.B Additional figures

In order to highlight possible parameter degeneracies we show in Fig. 5.10 all 2D projections of the parameters used in the most extended model ΛCDM+all (cf. Section 5.8.2 and Table 5.4).

Figures 5.11 and 5.12 show the additional contributions from a fiducial cosmological E-mode signal (EE, $z_2 \times z_1$ and EE, $z_2 \times z_2$) to all possible cross-terms (cf. Section 5.7).

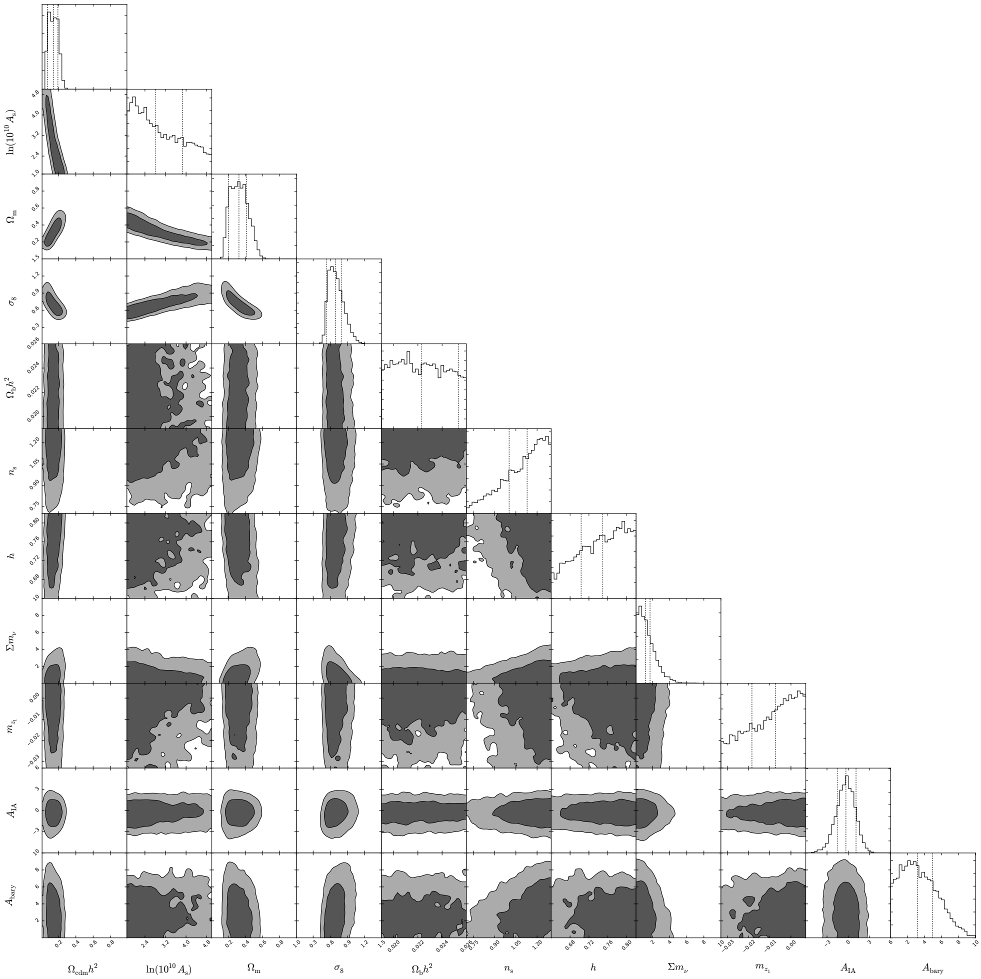

Figure 5.10: The parameter constraints derived from sampling the likelihood of model ΛCDM+all. The dashed lines in the marginalized 1D posteriors denote the weighted median and the 68 per cent credible interval (cf. Table 5.4). The contours in each 2D likelihood contour subplot are 68 and 95 per cent credible intervals smoothed with a Gaussian for illustrative purposes only.

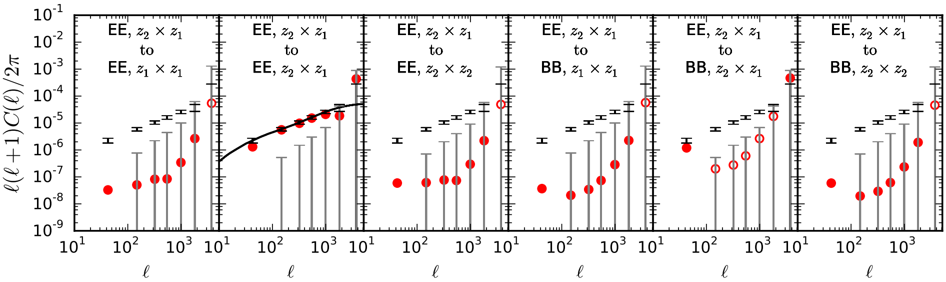

Figure 5.11: The contribution of a fiducial cosmological E-mode signal (solid, black line) for the redshift cross-correlation (i.e. $z_2 \times z_1$) convolved with the corresponding band window functions (red points) of all possible cross-combinations. The second panel from the left depicts the auto-contribution from (EE, $z_2 \times z_1$) to (EE, $z_2 \times z_1$). The grey errorbars show the statistical uncertainties associated with the B-modes. Open symbols denote negative values plotted at their absolute value.

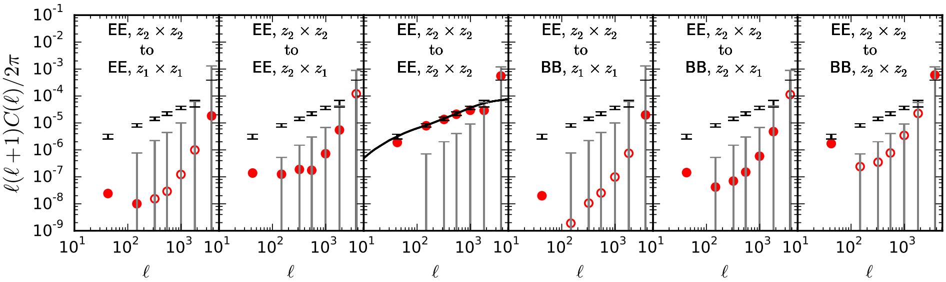

Figure 5.12: The contribution of a fiducial cosmological E-mode signal (solid, black line) for the high-redshift auto-correlation (i.e. $z_2 \times z_2$) convolved with the corresponding band window functions (red points) of all possible cross-combinations. The third panel from the left depicts the auto-contribution from (EE, $z_2 \times z_2$) to (EE, $z_2 \times z_2$). The grey errorbars show the statistical uncertainties associated with the B-modes. Open symbols denote negative values plotted at their absolute value.